2007-12-20

Lagrangian Coherent Structures and Transport in Two-Dimensional Incompressible Flows with Oceanographic and Atmospheric Applications

Irina I. Rypina
University of Miami, irypina@rsmas.miami.edu

UNIVERSITY OF MIAMI

LAGRANGIAN COHERENT STRUCTURES AND TRANSPORT IN TWO-DIMENSIONAL INCOMPRESSIBLE FLOWS WITH OCEANOGRAPHIC AND ATMOSPHERIC APPLICATIONS

By

Irina I. Rypina

A DISSERTATION

Submitted to the Faculty
of the University of Miami
in partial fulfillment of the requirements for
the degree of Doctor of Philosophy

Coral Gables, Florida

December 2007

UNIVERSITY OF MIAMI

A dissertation submitted in partial fulfillment of
the requirements for the degree of
Doctor of Philosophy

LAGRANGIAN COHERENT STRUCTURES AND TRANSPORT IN TWO-DIMENSIONAL INCOMPRESSIBLE FLOWS WITH OCEANOGRAPHIC AND ATMOSPHERIC APPLICATIONS

Irina I. Rypina

Approved:

Dr. Michael G. Brown Professor of Applied Marine Physics	Dr. Terri A. Scandura Dean of the Graduate School
Dr. William M. Drennan Professor of Applied Marine Physics	Dr. Thomas R. Hahn Professor of Applied Marine Physics
Dr. Maria J. Olascoaga Assistant Scientist	Dr. Huseyin Koçak Professor of Computer Science and Mathematics

RYPINA, IRINA I. (Ph.D., Applied Marine Physics)
(December 2007)

Lagrangian coherent structures and transport in two-dimensional incompressible flows with oceanographic and atmospheric applications

Abstract of a dissertation at the University of Miami.

Dissertation supervised by Professor Michael Brown.
No. of pages in text. (103)

The Lagrangian dynamics of two-dimensional incompressible fluid flows is considered, with emphasis on transport processes in atmospheric and oceanic flows. The dynamical-systems-based approach is adopted; the Lagrangian motion in such systems is studied with the aid of Kolmogorov-Arnold-Moser (KAM) theory, and results relating to stable and unstable manifolds and lobe dynamics. Some nontrivial extensions of well-known results are discussed, and some extensions of the theory are developed. In problems for which the flow field consists of a steady background on which a time-dependent perturbation is superimposed, it is shown that transport barriers arise naturally and play a critical role in transport processes. Theoretical results are applied to the study of transport in measured and simulated oceanographic and atmospheric flows. Two particular problems are considered. First, we study the Lagrangian dynamics of the zonal jet at the perimeter of the Antarctic Stratospheric Polar Vortex during late winter/early spring within which lies the "ozone hole". In this system, a robust transport barrier is found near the core of a zonal jet under typical conditions, which is responsible for trapping of the ozone-depleted air within the ozone hole. The existence of such a barrier is predicted theoretically and tested numerically with use of a dynamically-motivated analytically-prescribed model. The

second, oceanographic, application considered is the study of the surface transport in the Adriatic Sea. The surface flow in the Adriatic is characterized by a robust three-gyre background circulation pattern. Motivated by this observation, the Lagrangian dynamics of a perturbed three-gyre system is studied, with emphasis on intergyre transport and the role of transport barriers. It is shown that a qualitative change in transport properties, accompanied by a qualitative change in the structure of stable and unstable manifolds occurs in the perturbed three-gyre system when the perturbation strength exceeds a certain threshold. This behavior is predicted theoretically, simulated numerically with use of an analytically prescribed model, and shown to be consistent with a fully observationally-based model.

ACKNOWLEDGEMENTS

The work included in my Ph.D. dissertation at the University of Miami was carried out under the supervision of Prof. Michael G. Brown. Deep appreciation is expressed to him for his kind help, excellent scientific guidance, wise directions, and great care during the time of my doctoral work.

I would like to thank my other dissertation committee members, Dr. William M. Drennan, Dr. Thomas R. Hahn, Dr. Huseyin Koçak, and Dr. Maria J. Olascoaga for their input and discussions.

I would like also to acknowledge other researchers I have had the pleasure to interact with during my doctoral work: Dr. Francisco J. Beron-Vera and Ilya A. Udovydchenkov.

Table of Contents

List Of Figures

1 Introduction

Understanding transport and mixing processes in fluids is an important question that has been studied for many years. In the ocean transport by currents controls the distribution of water mass properties on a broad range of scales, from the global ocean scale to the microscale. Much of the work included in this dissertation focuses on the role of transport barriers. In addition to being interesting physical features with nontrivial dynamics, transport barriers have important biological implications and implications for pollutant dispersal. When investigating transport of passive tracers or fluid parcels it is most natural to adopt a Lagrangian point of view. The equation of motion for a particle passively advected by the Eulerian velocity field $\mathbf{u}(\mathbf{x}, t)$ is

$$\mathrm{d}\mathbf{x}/\mathrm{d}t = \mathbf{u}(\mathbf{x}, t). \tag{1}$$

Despite the simple form of Eq. (1), trajectories resulting from solving Eq. (1) may be very complex. In nonsteady 2D flows, even in the case of simple time-periodic flows, chaotic transport may occur.

In the ocean it is frequently assumed that there is a separation of scales between deterministic and stochastic components of the velocity field $\mathbf{u} = \mathbf{U} + \mathbf{u}'$, which leads to an advection-diffusion or Fokker-Planck equation to describe transport. The fluid particle trajectory is then controlled by two different processes: advection by the large scale velocity field $\mathbf{U}$ and turbulent transport by the small scale stochastic perturbation field $\mathbf{u}'$, which is characterized by an effective diffusivity. This approach, however, does not explain why mixing is enhanced in some regions and suppressed in

the others. Solving Eq. (1) numerically also does not answer this question.

An alternative approach to the study of fluid transport processes and Lagrangian fluid mechanics is to apply results associated with dynamical systems theory. Equation (1) defines a dynamical system. This system has a special form when the velocity field is two-dimensional $\mathbf{x} = (x, y)$ and incompressible. Then one can introduce a streamfunction $\psi(x, y, t)$ and the Lagrangian equations of motion are

$$\dot{x} = -\partial\psi/\partial y,\ \dot{y} = \partial\psi/\partial x. \tag{2}$$

It is well known that these equations have Hamiltonian form with streamfunction playing the role of Hamiltonian: $\psi(x, y, t) \leftrightarrow H(p, q, t)$. The Hamiltonian structure of Eqs. (2) will be discussed extensively later. We are interested in understanding both local and global dynamics in the phase space of the system, which in our case coincides with the actual physical space. We would like to separate regions of qualitatively different motion and characterize the transport between these regions. Dynamical systems tools allow identifying some structures in the flow of interest, called Lagrangian coherent structures (LCS) [1, 2, 3, 4, 5], which have major influence on the mixing of fluids. LCSs are material lines of fluid and as such represent impenetrable barriers to transport. Identification of LCSs is generally not possible from naked eye inspection of measured or simulated velocity fields or individual particle trajectories. Several techniques from dynamical systems theory have been developed and used to reveal LCSs in various oceanic and atmospheric flows [6, 7, 8]. The LCSs that are revealed are of two types. The first type, invariant stable and unstable manifolds

of nonstationary hyperbolic points, is associated with chaotic motion in regions with enhanced transport. The theory of lobe dynamics can be used to quantify chaotic transport in time-dependent flows [9, 10, 11, 12]. The second type of LCSs, called Kolmogorov-Arnold-Moser (KAM) invariant tori, is associated with regular or non-chaotic motion and regions with inhibited transport. Both types of transport barriers exist in nature. Transport barrier of the strong KAM stability type can be found, for example, at the perimeter of the southern hemisphere stratospheric polar vortex and is responsible for the trapping of the ozone-depleted air inside the "ozone hole" in the austral spring [7]. Another vivid example can be found in the atmosphere of Jupiter. The most striking feature of the Jovian atmosphere is a sequence of alternating regions, belts and zones, that have different radiative transfer properties. The existence of robust transport barriers associated with the strong KAM stability type between neighboring belts and zones explains the absence of fluid exchange between them [13]. A persistent transport barrier of the first type is present on the West Florida Shelf and is responsible for the existence of the so-called forbidden zone on the West Florida Shelf that is not visited by drifters that are released outside of this region [8].

With these comments as a background, we can state the objectives of this work. These objectives are: 1) to better understand and quantify transport processes in the oceanic and atmospheric flows; 2) to develop associated descriptive and predictive tools; and 3) to apply and test these tools using measured and simulated atmospheric and oceanic flows. Two applications will be in the focus of our study. The first one is concerned with the Lagrangian dynamics of the Stratospheric Polar Vortex and

is motivated by the desire to understand the mechanism by which ozone-depleted air is trapped within the ozone hole. The second application focuses on transport properties in a three-gyre system and is motivated by the desire to better understand transport in the Adriatic Sea, whose characteristic property is a well-defined three-gyre background circulation pattern.

This thesis is organized as follows. In Chapter 2 a brief description of the classical view on the transport problem is given, where the problem is treated as an advective-diffusive process. An alternative approach that explores techniques from the dynamical systems theory is presented in Chapter 3. Chapter 4 is concerned with Lagrangian dynamics of the Stratospheric Polar Vortex. In Chapter 5 transport in a three-gyre system is studied with application to the Adriatic Sea. In Chapter 6 a summary of the work presented is given.

2 Background. Advection-diffusion equation

The classical approach to understanding transport of fluids starts with the advection - diffusion equation that was first obtained by Einstein in the beginning of the twentieth century; derivation and analysis of this very basic result are given in Sec. 2.1. The work of Eckart is reviewed in Sec. 2.2, where the homogenization of two fluids is considered in more detail and three main stages of this process are identified. The advection-diffusion equation is seen to be a special case of a Fokker-Plank equation that describes a stochastic process. As a consequence, the diffusion process can be described by a stochastic differential equation, where the large scale mean flow is responsible for advection and a smaller scale turbulent velocity field plays the role of a random perturbation disturbing the system. A general review of stochastic differential equations and their connection to the advection-diffusion equation is given in Sec. 2.3.

2.1 Diffusion

In 1827 a botanist Robert Brown observed that suspended pollen grains are in uninterrupted and irregular motion. Being a botanist, he first believed that only organic materials exhibit this behavior but very soon he extended his observation to particles of inorganic matter. The cause of this Brownian motion was a subject of an intermittent discussion throughout the nineteenth century until in 1877 Delsaux suggested that the impact of molecules on a macroscopic particle produces observable displacements. In 1905, after almost a century of debate, Einstein gave an explanation of this phenomenon and derived the diffusion equation.

Einstein considered a one-dimensional Brownian motion by projecting the position of the particle onto a straight line, the x-axis. Two assumptions are necessary to proceed. First, particles are assumed to move independently from one another and, second, positions of particles are observed with time intervals τ that is much larger then the time interval between particle collisions. As a result, the motion of the particle during each time interval τ is independent from what happened in the previous intervals. In other words, the particle is involved into 1D random walk process, where the "walker" takes steps of random length Δ along the x-axis in a random direction. Denote the probability density of Δ by $\phi(\Delta)$, which is symmetric

$$\phi(\Delta) = \phi(-\Delta) \tag{3}$$

and normalized

$$\int_{-\infty}^{\infty} \phi(\Delta)\, d\Delta = 1. \tag{4}$$

Denote $c(x,t)$ the concentration of particles at time t. The evolution of $c(x,t)$ is then defined by the equation

$$c(x, t+\tau) = \int_{-\infty}^{\infty} c(x-\Delta, t)\, \phi(\Delta)\, d\Delta. \tag{5}$$

If the concentration is a slowly varying function of both time and space variables, with use of a Taylor series expansion, Eq. (5) can be approximated by

$$c(x,t) + c_t(x,t)\,\tau \approx \int_{-\infty}^{\infty} \phi(\Delta)\,[c(x,t) - c_x(x,t)\,\Delta + c_{xx}(x,t)\,\Delta^2/2] d\Delta. \tag{6}$$

With use of Eqs. (3) and (4), the above Eq. (6) can be further simplified to give the diffusion equation

$$c_t(x,t) \approx D c_{xx}(x,t), \tag{7}$$

where $D = \frac{\langle \Delta^2 \rangle}{2\tau}$ and $\langle\rangle$ denotes the expected value. Note that higher order terms in Taylor series expansion on the right-hand side of Eq. (6) lead to a hyper diffusive term $\widetilde{D} c_{xxxx}(x,t)$ on the right-hand side of Eq. (7). The advection-diffusion equation can be obtained from the diffusion equation Eq. (7) by using the total derivative, $d/dt = \partial/\partial t + (\mathbf{u} \cdot \nabla)$, instead of the partial derivative with respect to time, $\partial/\partial t$.

An alternative derivation of the diffusion equation Eq. (7) can be obtained with use of the Fick's law, which assumes that the substance goes from high density regions to low density regions,

$$\mathbf{J}(x,t) = -D(x) \nabla c(x,t). \tag{8}$$

Here $\mathbf{J}(x,t)$ represents the flux of a substance $c(x,t)$ and $D(x)$ is the diffusion coefficient. The balance law for an arbitrary region A dictates

$$\frac{d}{dt} \int_A c(x,t)\, dx = -\int_{\partial A} \mathbf{J}(x,t) \cdot \mathbf{n} d(\partial A) + \int_A f(x,t,c)\, dx, \tag{9}$$

where f represents the density of sources/sinks of c. With use of Eq. (8) and the divergence theorem, Eq. (9) becomes

$$\int_A \frac{\partial c(x,t)}{\partial t} dx = \int_A [\div (D(x) \nabla c(x,t)) + f(x,t,c)] dx. \tag{10}$$

Since the choice of the region A was arbitrary, the following diffusive differential

equation holds

$$\frac{\partial c\left(x,t\right)}{\partial t}dx = \div\left(D\left(x\right)\nabla c\left(x,t\right)\right) + f\left(x,t,c\right). \tag{11}$$

Below some basic properties of the diffusion process are described with use of the method of moments. A moment of order n of the concentration c is the integral of the form $\int_{-\infty}^{\infty} x^n c\left(x,t\right)dx$. The zeroth moment of the concentration $\int_{-\infty}^{\infty} c\left(x,t\right)dx$ is the total number of particles, $N\left(t\right)$; the first order moment of the concentration $\int_{-\infty}^{\infty} xc\left(x,t\right)dx$ is called the center of mass; and the second moment $\int_{-\infty}^{\infty} x^2 c\left(x,t\right)dx$ is called the moment of inertia or the mean square displacement of particles and is often denoted by $\langle x^2\rangle$. Taking the zeroth moment of Eq. (5) leads to the particle conservation law, $N\left(t+\tau\right) = N\left(t\right)$. Taking the first moment of the diffusion equation Eq. (5) leads to the stationarity of the center of mass, $\frac{d}{dt}\int_{-\infty}^{\infty} xc\left(x,t\right)dx = 0$. The second moment of the diffusion equation Eq. (5) describes the mean square displacement of particles, $\frac{d}{dt}\langle x^2\rangle = 2DN$. (We have assumed that terms $xc\left(x,t\right)$ and $x^2 c\left(x,t\right)$ vanish at $x \to \pm\infty$.) The last equation predicts the linear growth of the mean square displacement of particles in time. This equation is often taken as the defining characteristic of the diffusion process. Processes, in which the growth of the mean square displacement of particles is described by the power low $\langle x^2\rangle \sim t^m$ with $m \neq 1$ are referred to as "anomalous diffusion" processes (examples of anomalous diffusion processes can be found in [14, 15, 16, 17, 18]).

Another derivation of the advection-diffusion equation is presented below. As mentioned in the introduction, the stochastic approach to transport and mixing in fluid flows assumes a separation of scales between deterministic, $\mathbf{U}$, and stochastic,

$\mathbf{u}'$, components of the velocity field. The motion of fluid particles, Eq. (1), then dictates that

$$\mathrm{d}\mathbf{x}/\mathrm{d}t = \mathbf{U} + \mathbf{u}'. \tag{12}$$

For a phase space density function (or the trajectory density function in the case of 2D incompressible fluid flows, since the phase space of the system is the actual physical space where fluid motion takes place) $f(\mathbf{x}, t)$, which satisfies $\mathrm{d}f(\mathbf{x}, t)/\mathrm{d}t = 0$, the following equation holds (because $\mathrm{d}\mathbf{x}/\mathrm{d}t = \mathbf{u} = \mathbf{U} + \mathbf{u}'$):

$$\partial f/\partial t + \mathbf{U} \cdot \nabla f + \mathbf{u}' \cdot \nabla f = 0. \tag{13}$$

Similarly to the assumption of scale separation of the total velocity field, we assume that

$$f = \langle f \rangle + \delta f. \tag{14}$$

With use of this equation, Eq. (13) becomes

$$\partial\langle f\rangle/\partial t + \partial\delta f/\partial t + \mathbf{U} \cdot \nabla\langle f\rangle + \mathbf{U} \cdot \nabla\delta f + \mathbf{u}' \cdot \nabla\langle f\rangle + \mathbf{u}' \cdot \nabla\delta f = 0. \tag{15}$$

Direct averaging (taking the first moment) of Eq. (13) implies

$$\partial\langle f\rangle/\partial t + \mathbf{U} \cdot \nabla\langle f\rangle + \langle \mathbf{u}' \cdot \nabla f\rangle = 0. \tag{16}$$

With use of assumption Eq. (14), the last equation becomes

$$\partial\langle f\rangle/\partial t + \mathbf{U}\cdot\nabla\langle f\rangle + \langle \mathbf{u}'\cdot\nabla\langle f\rangle\rangle + \langle \mathbf{u}'\cdot\nabla\delta f\rangle = 0 \tag{17}$$

or, noting that $\langle \mathbf{u}'\cdot\nabla\langle f\rangle\rangle = \langle \mathbf{u}'\rangle\cdot\nabla\langle f\rangle = 0$,

$$\partial\langle f\rangle/\partial t + \mathbf{U}\cdot\nabla\langle f\rangle + \langle \mathbf{u}'\cdot\nabla\delta f\rangle = 0. \tag{18}$$

Combining Eqs. (16) and (18) yields the following equation

$$\partial\delta f/\partial t + \mathbf{U}\cdot\nabla\delta f = -\mathbf{u}'\cdot\nabla\langle f\rangle - \mathbf{u}'\cdot\nabla\delta f + \langle \mathbf{u}'\cdot\nabla\delta f\rangle. \tag{19}$$

Noting that the last 2 terms in the right-hand side of Eq. (19) cancel each other to the lowest order, Eq. (19) becomes

$$\mathrm{d}\delta f/\mathrm{d}t = (\partial/\partial t + \mathbf{U}\cdot\nabla)\,\delta f = -\mathbf{u}'\cdot\nabla\langle f\rangle. \tag{20}$$

or, in the integral form,

$$\delta f = -\int_0^t \mathbf{u}'\cdot\nabla\langle f\rangle \mathrm{d}t', \tag{21}$$

where the integration goes along the trajectory. Substituting Eq. (21) into Eq. (18) yields

$$\partial\langle f\rangle/\partial t + \mathbf{U}\cdot\nabla\langle f\rangle = \langle \mathbf{u}'\cdot\nabla\int_0^t \mathbf{u}'\cdot\nabla\langle f\rangle \mathrm{d}t'\rangle. \tag{22}$$

Now it is insightful to rewrite the right-hand side of Eq. (22) in the more explicit

notation

$$\langle \mathbf{u}'(\mathbf{x},t)\cdot\nabla\int_0^t \mathbf{u}'(\mathbf{x}(t'),t')\cdot\nabla\langle f(\mathbf{x}(t'),t')\rangle \mathrm{d}t'\rangle = \int_0^t \mathrm{d}t'\langle u_j'(\mathbf{x},t)\frac{\partial}{\partial x_j}\left(u_i'(\mathbf{x}(t'),t')\frac{\partial}{\partial x_i}\langle f(\mathbf{x}(t'),t')\rangle\right)\rangle. \tag{23}$$

Further simplification of Eq. (23) requires an additional assumption regarding the statistical properties of the turbulent velocity field $\mathbf{u}'$ to be made

$$\langle u_j'(\mathbf{x},t)\,u_i'(\mathbf{x}(t'),t')\rangle = \langle (u')^2\rangle\tau\delta_{ij}\delta(t-t') \tag{24}$$

where τ is the correlation time of the turbulent velocity field. Eq. (24) implies that for any times t and t', $u_j'(\mathbf{x},t)$ and $u_i'(\mathbf{x}(t'),t')$ have zero correlation when $i \neq j$. When $i = j$, the correlation between $u_j'(\mathbf{x},t)$ and $u_i'(\mathbf{x}(t'),t')$ is nonzero only at a zero time lag. In a strict mathematical sense, Eq. (24) is self-contradictory since it implies a zero correlation time τ. However, when τ is sufficiently small (which agrees with the scale separation assumption between the mean and turbulent components of the velocity field), one may expect Eq. (24) to be valid. In this case, by defining $\langle (u')^2\rangle\tau = D$, the advection-diffusion equation follows from Eq. (22)

$$\frac{\partial\langle f\rangle}{\partial t} + \mathbf{U}\cdot\nabla\langle f\rangle = \sqrt{D}\nabla\cdot\sqrt{D}\nabla\langle f\rangle. \tag{25}$$

2.2 Stirring and mixing

In this subsection the famous work of Eckart [19] is reviewed, where it is argued that, by analogy with the everyday experience of mixing cream into coffee, the homogenization of two fluids occurs in three stages. The distinction between the stages is made based on the value of the concentration gradient averaged over the domain. In the initial stage there are large distinct volumes of cream and coffee, inside which the gradient is small. Large gradients of concentration are present only on the interfaces between the two volumes. Thus, in the first stage the averaged over the entire domain gradient of the concentration is small. The intermediate stage, which is called stirring, is characterized by the increase in the average gradient as a result of stirring of liquids; the volumes of cream and coffee are distorted and the interfacial regions, where the gradient is large, increase in size. In the final stage, which is called mixing, gradients of concentration disappear and the liquid becomes homogeneous due to molecular diffusion. In general, early stages of the process, in which both stirring and mixing occur will be dominated by advective processes. Once the mean gradient has increased, however, diffusive processes start to dominate. Following the work of Eckart [19], the equation that governs the evolution of the mean square gradient in the advection-diffusion process can be derived. We start with the usual advection-diffusion equation

$$\frac{dc\left(x,t\right)}{dt} = D\frac{\partial^2 c\left(x,t\right)}{\partial x_i^2}, \tag{26}$$

where $\frac{dc(x,t)}{dt} = \frac{\partial}{\partial t} + u_i \frac{\partial}{\partial x_i}$ and the summation goes over the repeated indices. Applying

the ∇-operator to both sides of Eq.(26) yields

$$\frac{d}{dt}\frac{\partial c}{\partial x_j} = D\frac{\partial}{\partial x_j}\frac{\partial^2 c}{\partial x_i^2} - \frac{\partial u_i}{\partial x_j}\frac{\partial c}{\partial x_i}. \tag{27}$$

Multiplication of the last equation, Eq. (27), by $\partial c/\partial x_j$ and summation over the repeated indices leads to the following equation

$$\frac{1}{2}\frac{d}{dt}\left(\frac{\partial c}{\partial x_j}\right)^2 = D\frac{\partial}{\partial x_j}\left(\frac{\partial c}{\partial x_j}\frac{\partial^2 c}{\partial x_i^2}\right) - D\left(\frac{\partial^2 c}{\partial x_i^2}\right)^2 - \frac{\partial u_i}{\partial x_j}\frac{\partial c}{\partial x_i}\frac{\partial c}{\partial x_j}. \tag{28}$$

The integration of Eq. (28) over the material volume V that moves with the fluid gives

$$\frac{1}{2}\frac{dG^2}{dt} = \iint_{\partial V} \mathbf{n}\cdot\nabla c\frac{dc}{dt}d\left(\partial V\right) - DI^2 - S, \tag{29}$$

where

$$G^2 = \frac{1}{V}\iiint_V \left(\frac{\partial c}{\partial x_i}\right)^2 dV \tag{30}$$

defines the mean square gradient of the concentration in the volume V,

$$I^2 = \frac{1}{V}\iiint_V \left(\frac{\partial^2 c}{\partial x_i^2}\right)^2 dV \tag{31}$$

is a measure of inhomogeneity of the material inside the volume V, and

$$S = \frac{1}{V}\iiint_V \frac{\partial u_i}{\partial x_j}\frac{\partial c}{\partial x_i}\frac{\partial c}{\partial x_j}dV \tag{32}$$

determines the rate of change of the mean square gradient as a function of stirring.

Since usually stirring increases the mean square gradient of concentration, S is negative in most cases. In the case when the surface integral on the right-hand side of Eq. (29) and S vanish, the mean square gradient never increases.

2.3 A review of stochastic differential equations and their connection to the advection-diffusion equation

In the ocean it is often assumed that the velocity field has two distinct components, a large scale mean flow $\mathbf{U}$ and a small scale turbulent perturbation $\mathbf{u}'$. The connection to stochastic differential equations follows from Eq. (1) when $\mathbf{u}'$ is assumed to be a random perturbation to $\mathbf{U}$. Below we introduce the notion of a stochastic differential equation and stochastic integral. The simplest model for $\mathbf{u}'$ is an uncorrelated zero-mean stochastic process (white noise) $\xi(t)$. Equations of motion for a fluid particle starting from the initial position $\mathbf{x}(0) = \mathbf{x}_0$ are then given by Eq. (1)

$$\mathrm{d}\mathbf{x}/\mathrm{d}t = \mathbf{U}(\mathbf{x}, t) + \xi(t). \tag{33}$$

In the case when $\mathbf{U} = 0$ and $\mathbf{x}_0 = 0$, the solution to the previous equation is a so-called Wiener process, or Brownian motion, denoted by $\mathbf{W}(t)$: $\mathrm{d}\mathbf{W}/\mathrm{d}t = \xi(t)$. Equation (33) then becomes a stochastic differential equation

$$\mathrm{d}\mathbf{x}/\mathrm{d}t = \mathbf{U}(\mathbf{x}, t) + \mathrm{d}\mathbf{W}/\mathrm{d}t \tag{34}$$

or, after multiplying by $\mathrm{d}t$,

$$\mathrm{d}\mathbf{x} = \mathbf{U}(\mathbf{x}, t)\,\mathrm{d}t + \mathrm{d}\mathbf{W}. \tag{35}$$

Formally, one can rewrite the last equation as the stochastic integral of the form

$$\mathbf{x}(t) = \mathbf{x}_0 + \int_0^t \mathbf{U}(\mathbf{x}, t)\,\mathrm{d}t + \int_0^t \mathrm{d}\mathbf{W}. \tag{36}$$

The meaning of $\int_0^t \mathrm{d}\mathbf{W}$, however, is yet to be defined.

In order to define a stochastic integral of the form $\int_0^T G\mathrm{d}W$, where $G(t)$ is a stochastic process, following [20, 21, 22, 23], we first introduce the notion of a partition. The partition P of the interval $[0, T]$ is a finite collection of points $P \equiv [0 = t_0 < t_1 < \cdots < t_m = T]$ with the mesh size $|P| \equiv \max_{0<k<m-1} |t_{k+1} - t_k|$. For a given partition P and the number $0 < \lambda < 1$, the Riemann sum is defined as $R_n = (P, \lambda) \equiv \sum_{k=1}^{n-1} G((1-\lambda)\,t_k + \lambda t_{k+1})\,(W(t_{k+1}) - W(t_k))$. The stochastic integral is then defined as the limit $\int_0^T G\mathrm{d}W = \lim_{n\to\infty, |P|\to 0} R_n(P, \lambda)$. It can be shown [20] that $\lim_{n\to\infty,|P|\to 0} R_n(P, \lambda) = \frac{W(T)^2}{2} + \left(\lambda - \frac{1}{2}T\right)$, where the limit is taken in the mean square sense, $\langle \left(R_n - \frac{W(T)^2}{2} + \left(\lambda - \frac{1}{2}\right) T \right)^2 \rangle \to 0$. This limit and, consequently, the value of the stochastic integral depend on the choice of λ. The Ito definition corresponds to the choice of $\lambda = 0$. (An alternative definition, due to Stratonovich, corresponds to $\lambda = 1/2$.) According to the Ito definition, stochastic integral

$$\int_0^t W\mathrm{d}W = \frac{W(t)^2}{2} - \frac{t}{2}. \tag{37}$$

The last Eq. (37) is known as Ito's formula. Another key formula of stochastic calculus is Ito's chain rule: let $\mathrm{d}x = F\mathrm{d}t + G\mathrm{d}W$ and $y(t) = y(x(t), t)$, then

$$\mathrm{d}y = \frac{\partial y}{\partial t}\mathrm{d}t + \frac{\partial y}{\partial x}\mathrm{d}x + \frac{1}{2}\frac{\partial^2 y}{\partial x^2}G^2\mathrm{d}t. \tag{38}$$

We return now to the stochastic differential equation Eq. (35). Using the chain rule Eq. (38) for an arbitrary function $f(x)$

$$\mathrm{d}f = \frac{\partial f}{\partial x}\mathrm{d}x + \frac{1}{2}\frac{\partial^2 f}{\partial x^2}\mathrm{d}t = \left(\frac{\partial f}{\partial x}U + \frac{1}{2}\frac{\partial^2 f}{\partial x^2}\right)\mathrm{d}t + \frac{\partial f}{\partial x}\mathrm{d}W. \tag{39}$$

It follows from the last equation that

$$\frac{\langle \mathrm{d}f\rangle}{\mathrm{d}t} = \langle \frac{\partial f}{\partial x}U + \frac{1}{2}\frac{\partial^2 f}{\partial x^2}\rangle. \tag{40}$$

Let $p(x,t)$ denote the probability density function of x. With use of the equality $\frac{\langle \mathrm{d}f\rangle}{\mathrm{d}t} = \frac{\mathrm{d}}{\mathrm{d}t}\langle f\rangle$ it follows from Eq. (40) that

$$\int f\frac{\partial p}{\partial t}\mathrm{d}x = \int \left[\frac{\partial f}{\partial x}U + \frac{1}{2}\frac{\partial^2 f}{\partial x^2}\right]p\mathrm{d}x. \tag{41}$$

Integrating by parts and discarding surface terms gives

$$\int f\frac{\partial p}{\partial t}\mathrm{d}x = \int f\left[-\frac{\partial (Up)}{\partial x} + \frac{1}{2}\frac{\partial^2 p}{\partial x^2}\right]\mathrm{d}x. \tag{42}$$

Since the choice of $f(x)$ is arbitrary, the following equation should hold for any x and t:

$$\frac{\partial p}{\partial t} = -\frac{\partial (Up)}{\partial x} + \frac{1}{2}\frac{\partial^2 p}{\partial x^2}. \tag{43}$$

We recognize the last equation as the advection-diffusion equation with diffusivity $D = 1$. This is a special case of a more general Fokker-Planck equation in the theory of stochastic differential equations.

To summarize, the main concept of the stochastic view on transport in 2D fluid flows is given below. In this approach, the flow field is decomposed into a large scale mean velocity $\mathbf{U}$ and a small scale perturbation $\mathbf{u}'$. Such decomposition of the flow field leads to a Fokker-Planck equation that describes the space-time evolution of the particle probability density function. This equation can also be thought of as an advection-diffusion equation for concentration of a passive tracer. The corresponding particle trajectory (Langevin) equations constitute a system of stochastic differential equations; the small-scale velocity field $\mathbf{u}'$ is treated as a stochastic process (such as, for example, a Markov process satisfying the random-flight model [24]), the parameters of which need to be estimated statistically from available data sets. Such statistical approach has been used extensively in a number of oceanographic studies ([25, 26, 27, 28, 29]). The fundamental difficulty relevant to all of these studies is that in realistic (turbulent) fluid flows many interacting processes act simultaneously over a wide range of scales. As a result, it may be very difficult to estimate parameters for use in the corresponding stochastic model that adequately represent all these interaction scales. Also, it is difficult to reconcile transport barriers, as described in the following sections, with a stochastic/diffusive description of transport.

3 Overview of relevant dynamical systems results

This chapter is devoted to the dynamical systems view of transport and mixing in fluids. The fluid flow is assumed to be two-dimensional and incompressible; the associated Lagrangian equations of motion then have Hamiltonian form and the phase space of a system and the physical space, where the motion takes place, coincide with each other. The identification of barriers to transport will be an important focus of our study. Techniques from dynamical systems theory can be applied to reveal such barriers. An overview of relevant dynamical systems techniques is given in this section. The revealed barriers are of two types: the first type is associated with invariant stable and unstable manifolds of nonstationary hyperbolic points in the flow of interest. The second type is associated with surviving KAM invariant tori; barriers of this type are often found near cores of jet-like structures. Often these are associated with the phenomenon of "strong KAM stability" as described below. Both types of transport barriers can be described as a Lagrangian coherent structures in dynamical systems theory.

This chapter is organized as follows. In Sec. 3.1 steady (time-independent) fluid flows are considered and action-angle variables are introduced. In Sec. 3.2 periodically-perturbed fluid flows are studied. A review of lobe dynamics is given in Sec. 3.3, where the notion of stable and unstable invariant manifold of nonstationary hyperbolic points is introduced. Sec. 3.4 is concerned with estimating flux in regions with chaotic behavior with use of the global perturbation method called the Melnikov method. A numerical technique called the double time-slice method that can be used

to estimate stable and unstable manifolds is explained in Sec. 3.5. The notion of Lyapunov exponent is introduced and discussed in Sec. 3.6. In Sec. 3.7 a finite-time generalization of Lyapunov exponent is introduced, the finite-time Lyapunov exponent (FTLE), that is applicable to finite-time samples in real fluid flows with general time-dependence. The notion of fractal dimension - a commonly exploited manifestation of fractal behavior of trajectories - is discussed in Sec. 3.8, where a numerical algorithm for estimating fractal dimension of trajectory from a set of discrete samples is explained. Subsection 3.9 is devoted to the discussion of the famous Kolmogorov-Arnold-Moser (KAM) theorem including several nontrivial extensions of the basic result. These are concerned with the applicability of the theorem when the usual statements of nondegeneracy condition are violated and applicability of the theorem to multiply-periodic systems. In Sec 3.10 systems that locally violate the twist condition are considered and the "strong KAM stability" phenomenon near shearless tori is discussed. Transport barriers in unsteady 2d incompressible flows can be characterized as Lagrangian Coherent Structures (LCS). In Sec. 3.11 the notion of LCS is introduced and numerical techniques are discussed that allow extracting LCS from measured or simulated velocity fields.

3.1 Steady 2D incompressible fluid flows

We are interested in the motion of fluid particle or passive tracers in 2D incompressible fluid flows. The Lagrangian equations of motion are given by the system of Hamilton's equations, Eq. (2), with streamfunction $\psi(x, y, t)$ playing the role of Hamiltonian $H(p, q, t)$. For any steady flow $\psi(x, y)$ it follows from Eq. (2) that

$\mathrm{d}\psi/\mathrm{d}t = 0$ following the trajectory. The motion in this case is completely integrable and fluid particle trajectories coincide with streamlines of the flow. This means that chaotic motion cannot occur in such systems and all the trajectories are regular (non-chaotic) curves in (x, y) space.

The analysis of such a system is most conveniently described in terms of action-angle variables (I, θ). The equations of motion in action-angle form maintain its Hamiltonian structure with $H(I) = \psi(x, y)$

$$\dot{I} = -\frac{\partial H(I)}{\partial \theta} = 0,\ \dot{\theta} = \frac{\partial H(I)}{\partial I} = \omega(I). \tag{44}$$

These equations can be trivially integrated to give $I = \text{const}$ following the trajectory and $\theta(t) = \theta_0 + \omega(I)\, t$. Thus, action I is simply a label for a particular trajectory and the motion is 2π-periodic in θ with angular frequency $\omega(I)$. The period of motion is connected to the angular frequency of motion in the usual fashion, $T(I) = 2\pi/\omega(I)$. The quantity $\omega'(I) = d\omega/dI$, which is a measure of shear on a particular trajectory, will be very important in our later discussion. The trajectory satisfying the condition $\omega'(I) = 0$ is referred to as shearless. (Also, terms twistless or degenerate are often used.)

The canonical transformation that relates the old variables (x, y) to the new action-angle variables (I, θ) with $\psi(x, y) = H(I)$ is accomplished through the generating function

$$G(y, I) = \int^{y} x(y', H)\, dy'. \tag{45}$$

Action and angle variables are then defined as follows

$$I(H) = (2\pi) \oint x(y, H)\, dy,\ \theta = \partial G/\partial I. \tag{46}$$

Details of this canonical transformation are well-known [30] and will not be further discussed here. In many cases, it is necessary to introduce action-angle variables in different regions of the (x, y) space in a piecewise fashion. Once it is done, however, the equations of motion in each region are given by Eq. (44).

3.2 2D incompressible fluid flows with periodic time-dependence

In this section Hamiltonian systems of the form Eq. (2) with bounded phase space (x, y) and $2\pi/\sigma$-periodic in t streamfunction

$$\psi = \psi(x, y, \sigma t) \tag{47}$$

are considered. As mentioned in the introduction, even in the simple time-periodic case chaotic motion may occur and trajectories resulting from Eqs. (2) and (47) may be quite complicated. Trajectories in such systems lie in 3D phase space $(x, y, t \bmod 2\pi)$. At that, regular trajectories lie on tori in the 3D phase space (these are so-called KAM invariant tori) and chaotic trajectories fill volumes between these tori. Each torus is a 2D surface that divides the 3D phase space into two disjoint regions - the well-defined inside and outside. As such, each torus represents an impenetrable barrier to transport of passive tracers in time-periodic flows.

3.2.1 Poincare section

The usual way to view trajectories in 2D incompressible time-periodic fluid flows is to construct a Poincare section. A Poincare section reduces the study of continuous fluid flows to the study of area preserving maps. A Poincare section is the technique that allows to view trajectories in 2D space by taking a slice of 3D phase space corresponding to fixed value of t mod 2π. To do so, one samples trajectory stroboscopically after each period of time, i.e., at discrete set of times $t = t_0 + 2\pi n/\sigma$, where $n = 1, 2, \cdots$. Specific quantitative features of the Poincare section depend on the choice of the staring time t_0, however, Poincare sections for different t_0 have similar qualitative structure. Because each regular trajectory lies on the torus in 3D phase space, it appears as a discretely sampled smooth curve on the Poincare section. Chaotic trajectories fill volumes in 3D phase space, consequently they appear as sets of scattered dots that fill areas on the Poincare section. Since the space (x, y) is the actual physical space where fluid motion takes place, water is well-mixed inside each chaotic region of the Poincare section. Regular trajectories lie on KAM invariant tori, which act as barriers and prevent mixing of water between different disjoint chaotic regions of the Poincare section.

3.3 Lobe dynamics

Chaotic motion is characterized by extreme sensitivity to initial positions of fluid particles, which means that neighboring fluid particles separate from each other at an exponential rate. Simultaneously, a compact blob of fluid particles or passive

tracers will disperse throughout the chaotic region in such a way that the area of the blob is conserved (this is a consequence of the incompressibility assumption). In a bounded domain this is accomplished by repeated stretching and folding of fluid elements; this process is linked to the existence of Smale horseshoes. This process is called chaotic mixing. Lobe dynamics theory [31, 32, 33, 34, 10, 9] allows one to characterize this process by determining special material curves, stable and unstable manifolds of generally nonstationary hyperbolic points, that act as a template for chaotic mixing.

First, consider a saddle-type stagnation point (a stationary hyperbolic point) of a steady flow. The saddle-type nature of the stagnation point is determined by the eigenvalues of the constant matrix which describes the linearized flow field in the vicinity of the stagnation point. Associated with this stationary hyperbolic point are stable and unstable invariant manifolds. In the case of a steady flow, stable and unstable manifolds coincide with actual fluid particle trajectories. Along the stable manifolds fluid particles exponentially approach the hyperbolic point in forward time; along the unstable manifolds fluid particles exponentially approach the hyperbolic point in backward time. In steady flows, stable and unstable manifolds fall on top of each other forming homoclinic (or heteroclinic) trajectories, which act as separatrices that separate regions of qualitatively different motion from each other.

For fluid flows with periodic time dependence, with period T, the notion of a stationary hyperbolic point of a flow is replaced by the notion of a stationary hyperbolic point of the corresponding area-preserving map on the Poincare section. These are constructed by sampling trajectories at $t = t_0 + nT$, $n = 1, 2, \ldots$ (see Sec. 3.2 for

details). Associated with this hyperbolic stationary point of a map there exist a corresponding stable and unstable invariant manifolds, which, unlike the steady flow case, do not coincide with each other but rather intersect transversally forming homoclinic (or heteroclinic) tangles. Since the Poincare section depends on the particular choice of t_0, the position of the hyperbolic point (and, consequently, the corresponding stable and unstable invariant manifolds) in the Poincare section also depends on t_0. (The existence of the hyperbolic point does not, however, depend on the choice of t_0, i.e., if the hyperbolic point is present for one t_0, it is present for all t_0.)

The generalization of the hyperbolic stationary point for unsteady flows with aperiodic time dependence gives rise to the notion of the hyperbolic (or saddle-type) trajectory, $\gamma(t)$, in the extended phase space (x, y, t). The saddle-type nature of such hyperbolic trajectory is also determined from the linearization of the flow about the hyperbolic trajectory. However, in this case, the definition of the hyperbolic trajectory is more complex because the eigenvalues of the time dependent matrix associated with the linearized velocity field cannot generally be used to determine the saddle-type nature of the trajectory. A rigorous mathematical definition of the hyperbolic trajectory can be found in [34]. Physically, one can think of a hyperbolic trajectory as a "moving saddle-point". The stable and unstable manifold theorem for hyperbolic trajectories [34, 35] states that, associated with the hyperbolic trajectory in the extended phase space (x, y, t), there exist stable and unstable invariant manifolds, $W^s(\gamma(t))$ and $W^u(\gamma(t))$, which possess the following properties: 1) projections of $W^s(\gamma(t))$ and $W^u(\gamma(t))$ to (x, y) space are moving invariant curves (corresponding physically to material lines of fluid), so that particle trajectory cannot cross them;

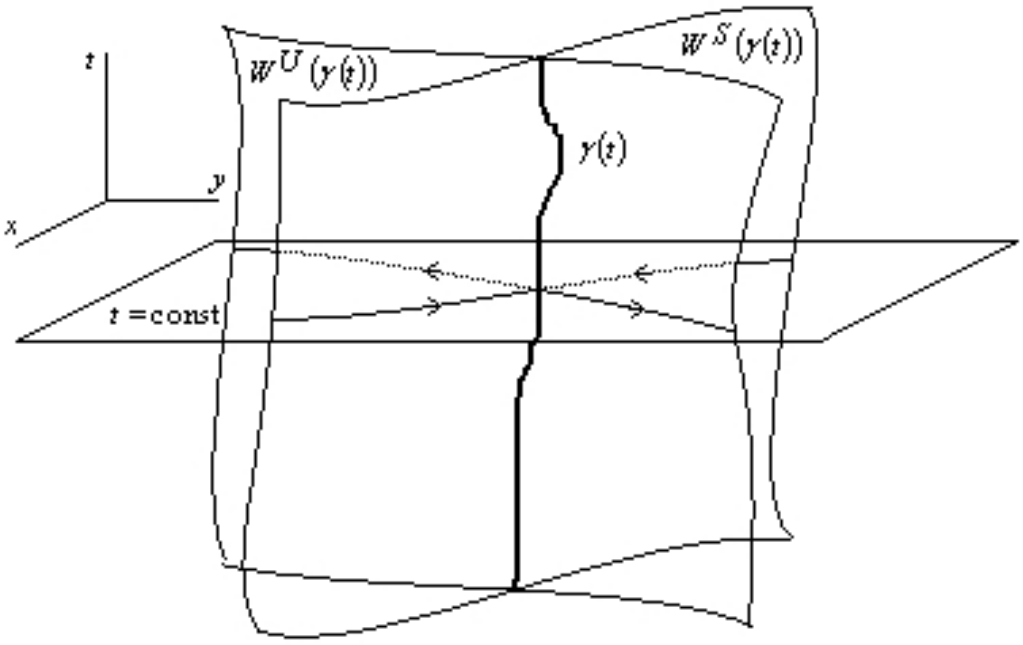

Figure 1: Geometry of the stable and unstable manifolds of hyperbolic trajectory in the extended phase space (x, y, t) and on a time slice $t = \text{const}$.

and 2) particle trajectories that start on the stable manifold approach the hyperbolic trajectory at an exponential rate as $t \to \infty$; particle trajectories that start on the unstable manifold approach the hyperbolic trajectory at an exponential rate as $t \to -\infty$.

Below we discuss the implications of stable and unstable manifolds of hyperbolic trajectories for transport, starting with the definition of the primary intersection point between stable and unstable manifolds on a time slice, $t = \text{const}$. The geometry of the stable and unstable manifolds of a hyperbolic trajectory in the extended phase space (x, y, t) and on a time slice $t = \text{const}$ is shown in Fig. 1. The intersection point between stable and unstable manifolds is called the primary intersection point $\left(x^{PIP}, y^{PIP}\right)$ if a segment of the stable manifold from the hyperbolic point to the intersection point $\left(x^{PIP}, y^{PIP}\right)$ and a segment of the unstable manifold from the hy-

perbolic point to the intersection point $\left(x^{PIP}, y^{PIP}\right)$ intersect each other only at the point $\left(x^{PIP}, y^{PIP}\right)$. Closed regions trapped between segments of stable and unstable manifolds, bounded by two neighboring primary intersection points, are called lobes. Because segments of stable and unstable manifold forming a lobe constitute barriers to transport, fluid particles are trapped inside the lobe and constrained to move with the lobe. Intersection points belong both to stable and unstable manifolds. Hence, they approach nonstationary hyperbolic point along stable/unstable manifold in forward/backward time. During this process, the segment of the stable/unstable manifold that bounds a lobe decreases in length, while the segment of the unstable/stable manifold increases in length. As a result, lobes transform into long filaments in such a way that the area of the lobe is conserved. This is the mechanism by which chaotic mixing occurs.

Segments of stable and unstable manifolds from the hyperbolic point to their first primary intersection point (that is called boundary intersection point (BIP)) form a well-defined boundary that divides the phase plane (x, y) into two disjoint regions. Figure 2 illustrates schematically the geometry of intersecting stable and unstable manifolds of hyperbolic trajectories, lobes and BIP on the time slice $t = t_0$. Because stable and unstable manifolds evolve in time, the boundary formed by their segments also deforms as time progresses. Thus, at two different times the boundary is different. However, at any given time $t = \text{const}$ the boundary is well-defined. Lobe dynamics theory predicts [31, 32, 33, 34, 10, 9] that the only points that can cross such a boundary, formed by segments of stable and unstable manifolds, are contained in lobes produced by these invariant manifolds. Also, lobe dynamics predicts the order

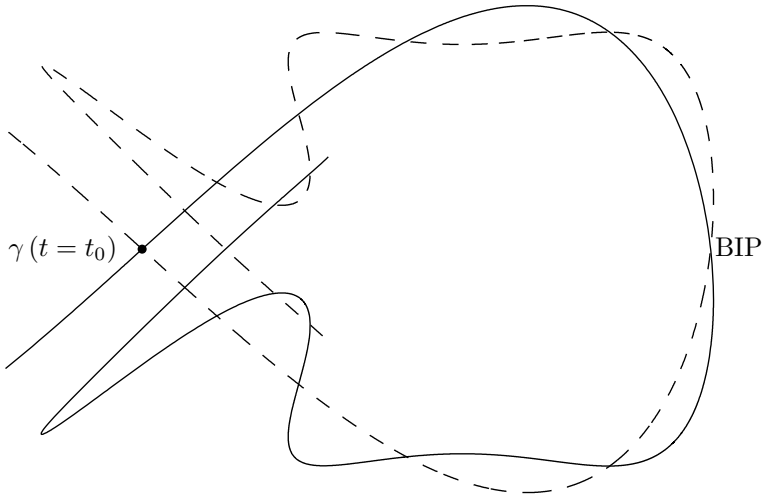

Figure 2: Schematic diagram showing intersecting stable and unstable manifolds of hyperbolic trajectory $\gamma\,(t)$, lobes and the boundary intersection point (BIP) on a time slice $t = t_0$.

in which lobes will cross the boundary, this is the so-called turnstile mechanism. These two predictions allow one to quantify flux of fluid or passive tracers across the boundary and thus characterize transport.

For streamfunctions of the form Eq. (47), due to time-periodicity of the perturbation, the manifold structure and consequently the boundary produced by segments of invariant manifolds is constrained to repeat itself after each period $T = 2\pi/\sigma$. In such systems, lobes cross the boundary in pairs, one lobe going from the inside of the boundary to the outside, the other - from the outside to the inside. This has two consequences: first, after one period of the perturbation, the flux across the boundary consists of fluid contained in one lobe and, second, the area of all lobes is the same because of the incompressibility (or area preservation) condition. The corresponding behavior of non-time-periodic flows is more complicated.

3.4 Melnikov method

For two-dimensional incompressible time dependent flows given by Eq. (2) with the streamfunction of the form $\psi(x,y,t) = \psi_0(x,y) + \epsilon\psi_1(x,y,t)$ where $\epsilon \ll 1$, the area of the lobe can be computed with use of a global perturbation method, called Melnikov's method [36, 31, 34, 37]. The advantage of this method is that if the form of the streamfunction is known, it only requires the knowledge of the unperturbed homoclinic (or heteroclinic) trajectory $\left(x^h(t), y^h(t)\right)$ and does not require the computation of stable and unstable manifolds. The Melnikov function

$$M(t_0) = \epsilon \int_{-\infty}^{\infty} \left(\frac{\partial\psi_0}{\partial x}\frac{\partial\psi_1}{\partial y} - \frac{\partial\psi_0}{\partial y}\frac{\partial\psi_1}{\partial x} \right) |_{\left(x^h(t-t_0), y^h(t-t_0), t\right)} \, \mathrm{d}t \tag{48}$$

provides an $O(\epsilon)$ - estimate for the distance between the stable and unstable manifolds on the nonstationary hyperbolic point. Zeros of the Melnikov function correspond to primary intersection points of stable and unstable manifolds. The area of the lobe bounded by intersection points t_1^{PIP} and t_2^{PIP} is given by

$$A = \left| \int_{t_1^{PIP}}^{t_2^{PIP}} M(t_0)\, \mathrm{d}t_0 \right| + O\left(\epsilon^2\right). \tag{49}$$

Two-dimensional flux of fluid across the corresponding segment of the boundary is then given by $F = A/\Delta t$ where Δt is time required for the lobe to cross the boundary.

3.5 Double time-slice method

A numerical technique that is commonly used to compute stable and unstable invariant manifolds in unsteady flows is called the double time-slice method [34].

It requires evolving a set of initial conditions surrounding the hyperbolic point forward and backward in time during some integration interval. At that, because of rapid stretching of a set of initial conditions in the direction of stable/unstable manifold, some care is required to maintain the resolution at longer integration intervals. In numerical computations, a seeding procedure is often implemented to produce smoothly resolved long enough segments of stable and unstable manifolds. An alternative technique that is capable of detecting transport barriers involves computation of finite-scale (FSLE) or finite-time (FTLE) Lyapunov exponents. It will be discussed in detail further in text.

3.6 Lyapunov exponents

The distinction between regular motion and chaotic motion is often quantified with use of Lyapunov exponents. Lyapunov exponent provide a measure of rate at which initially nearby trajectories diverge from each other under the influence of fluid flow. The formal definition of the Lyapunov exponent λ is the following

$$\lambda = \lim_{t\to\infty} \lim_{d_0\to 0} \frac{1}{t} \ln \frac{d\,(t)}{d_0}, \tag{50}$$

where $d\,(t)$ is a suitably chosen measure of distance between two trajectories and $d_0 = d\,(t=0)$. Since chaotic motion is characterized by sensitivity to initial conditions, chaotic trajectories diverge from each other at exponential rate and are characterized by positive Lyapunov exponents. In regions that do not include hyperbolic points and homoclinic or heteroclinic trajectories, regular trajectories diverge at polynomial rate and correspond to $\lambda = 0$. Eq. (50) involves two limits and is not suitable for

numerical calculation of Lyapunov exponents. The elimination of one limit ($\lim_{d_0 \to 0}$) is possible with use of variational equations. Consider the evolution of the initial infinitesimal perturbation $(\delta x_0, \delta y_0)$ to trajectory starting with (x_0, y_0) in the flow Eq. (2). To the lowest order in $(\delta x_0, \delta y_0)$,

$$\begin{pmatrix} \delta x \\ \\ \delta y \end{pmatrix} = Q \begin{pmatrix} \delta x_0 \\ \\ \delta y_0 \end{pmatrix}, \tag{51}$$

where Q is the Jacobian matrix of the associated flow often refered to as the stability matrix

$$Q = \begin{pmatrix} \frac{\partial x}{\partial x_0} & \frac{\partial x}{\partial y_0} \\ \\ \frac{\partial y}{\partial x_0} & \frac{\partial y}{\partial y_0} \end{pmatrix}. \tag{52}$$

It follows from Eq. (2) that the elements of the stability matrix evolve according to

$$\frac{\mathrm{d}Q}{\mathrm{d}t} = JQ, \tag{53}$$

with initial condition

$$Q\left(0\right) = I \tag{54}$$

where and I is the identity matrix and J is the Jacobian matrix of the Hamiltonian vector field

$$J = \begin{pmatrix} \frac{-\partial^2 \psi}{\partial x \partial y} & \frac{-\partial^2 \psi}{\partial y^2} \\ \\ \frac{\partial^2 \psi}{\partial x^2} & \frac{\partial^2 \psi}{\partial x \partial y} \end{pmatrix}. \tag{55}$$

Let now $\lambda^Q\left(t\right)$ be the largest of two eigenvalues of Q and consider the following

definition (see, e.g. [38])

$$\lambda = \lim_{t\to\infty} \frac{1}{t} \ln \left|\lambda^Q\right|. \tag{56}$$

If the limit in Eq. (56) exists and is not zero, then

$$(\delta x, \delta y) \sim \exp \lambda t \tag{57}$$

i.e., nearby trajectories diverge exponentially in time. Hence, Eq. (56) can be taken as a suitable definition of the Lyapunov exponent.

The geometrical interpretation of equation Eq. (56) will now be given. The variational equations describe the evolution of an infinitesimal circle in the flow. This circle gets deformed into an ellipse under the influence of the flow. During this process, the area of the ellipse is conserved and equal to the area of the initial circle due to the incompressibility of the flow (Liouville's theorem [39, 40] guarantees that the area is preserved in the phase space leading to the condition $\det Q = 1$). The eigenvectors of Q define the orientation of the ellipse and the largest eigenvalue λ^Q is a measure of the semimajor axis of the ellipse. Hence, it is a suitable choice of the distance d in Eq. (50). In highly chaotic flows, an initial circle tends to align along the semimajor axis associated with the largest eigenvalue λ^Q very quickly. As a result, matrix Q becomes ill-conditioned very quickly and λ^Q (and, consequently, λ) can not be computed reliably at long times. Several techniques can be used to overcome this problem.

Following [41, 42], let $A(t)$ be the bounded-element matrix such that

$$Q = A \exp \lambda_{guess} t. \tag{58}$$

Consequently

$$\lambda^Q = \lambda^A \exp \lambda_{guess} t \tag{59}$$

where λ_{guess} is a guessed value of λ. It follows from the variational equation Eq. (53) that the evolution of A is given by the following equation

$$\frac{\mathrm{d}A}{\mathrm{d}t} = \left(J - \lambda_{guess} I\right) A \tag{60}$$

with the initial condition

$$A(0) = I. \tag{61}$$

If λ_{guess} is close to λ, the matrix A remains well-conditioned at much longer times then the matrix Q.

Another approach to overcome the problem of elements of Q becoming ill-conditioned involves successive renormalization of the elements of Q after some interval of time T when integrating simultaneously Eqs. (2) and (53) [38]. Let $\boldsymbol{\delta}\mathbf{x_0} = (\delta x_0, \delta y_0)$ be the initial perturbation to the point $\mathbf{x_0} = (x_0, y_0)$ and define the 0-th iteration as follows

$$\boldsymbol{\delta}\mathbf{x}^{(\mathbf{0})} = \boldsymbol{\delta}\mathbf{x_0},\ \mathbf{u}^{(\mathbf{0})} = \boldsymbol{\delta}\mathbf{x_0} / \left|\boldsymbol{\delta}\mathbf{x_0}\right|,\ \mathbf{x}^{(\mathbf{0})} = \mathbf{x_0}. \tag{62}$$

Let $\phi_T(\mathbf{x})$ denote the flow map that advances fluid particles from their initial position

at time t to their final position at time $t+T$. The first iteration is then defined as

$$\begin{aligned} \boldsymbol{\delta}\mathbf{x}^{(\mathbf{1})} &= \boldsymbol{\delta}\mathbf{x}\left(T;\mathbf{u}^{(\mathbf{0})},\mathbf{x}^{(\mathbf{0})}\right)=\phi_T\left(\mathbf{x}^{(\mathbf{0})}\right)\mathbf{u}^{(\mathbf{0})}, \\ \mathbf{u}^{(\mathbf{1})} &= \boldsymbol{\delta}\mathbf{x}^{(\mathbf{1})}/\left|\boldsymbol{\delta}\mathbf{x}^{(\mathbf{1})}\right|. \end{aligned} \tag{63}$$

The second iteration is defined as

$$\boldsymbol{\delta}\mathbf{x}^{(\mathbf{2})}=\boldsymbol{\delta}\mathbf{x}\left(2T;\mathbf{u}^{(\mathbf{0})},\mathbf{x}^{(\mathbf{0})}\right)=\phi_{2T}\left(\mathbf{x}^{(\mathbf{0})}\right)\mathbf{u}^{(\mathbf{0})}=\phi_{2T}\left(\mathbf{x}^{(\mathbf{0})}\right)\mathbf{x}^{(\mathbf{0})}\frac{1}{\left|\boldsymbol{\delta}\mathbf{x}^{(\mathbf{0})}\right|}= \tag{64}$$

$$\phi_T\left(\mathbf{x}^{(\mathbf{1})}\right)\phi_T\left(\mathbf{x}^{(\mathbf{0})}\right)\mathbf{x}^{(\mathbf{0})}\frac{1}{\left|\boldsymbol{\delta}\mathbf{x}^{(\mathbf{0})}\right|}=\phi_T\left(\mathbf{x}^{(\mathbf{1})}\right)\boldsymbol{\delta}\mathbf{x}^{(\mathbf{1})}\left|\boldsymbol{\delta}\mathbf{x}^{(\mathbf{0})}\right|\frac{1}{\left|\boldsymbol{\delta}\mathbf{x}^{(\mathbf{0})}\right|}=\phi_T\left(\mathbf{x}^{(\mathbf{1})}\right)\boldsymbol{\delta}\mathbf{x}^{(\mathbf{1})}=$$

$$\boldsymbol{\delta}\mathbf{x}^{(\mathbf{2})}\left|\boldsymbol{\delta}\mathbf{x}^{(\mathbf{1})}\right|=\mathbf{u}^{(\mathbf{2})}\left|\boldsymbol{\delta}\mathbf{x}^{(\mathbf{2})}\right|\left|\boldsymbol{\delta}\mathbf{x}^{(\mathbf{1})}\right|,$$

$$\mathbf{u}^{(\mathbf{2})}=\boldsymbol{\delta}\mathbf{x}_{\mathbf{2}}/\left|\boldsymbol{\delta}\mathbf{x}_{\mathbf{2}}\right|$$

and the k-th iteration as

$$\boldsymbol{\delta}\mathbf{x}^{(\mathbf{k})}=\boldsymbol{\delta}\mathbf{x}\left(kT;\mathbf{u}^{(\mathbf{0})},\mathbf{x}^{(\mathbf{0})}\right)=\mathbf{u}^{(\mathbf{k})}\left|\boldsymbol{\delta}\mathbf{x}^{(\mathbf{k})}\right|\cdots\left|\boldsymbol{\delta}\mathbf{x}^{(\mathbf{1})}\right|,$$

$$\mathbf{u}^{(\mathbf{k})}=\boldsymbol{\delta}\mathbf{x}_{\mathbf{k}}/\left|\boldsymbol{\delta}\mathbf{x}_{\mathbf{k}}\right| \tag{65}$$

In the case when k is sufficiently large, the Lyapunov exponent λ can be approximated as follows

$$\lambda\approx\frac{1}{kT}\ln\left|\boldsymbol{\delta}\mathbf{x}\left(kT;\mathbf{u}^{(\mathbf{0})},\mathbf{x}^{(\mathbf{0})}\right)\right|=\frac{1}{kT}\ln\prod_{k=1}^{k}\left|\boldsymbol{\delta}\mathbf{x}^{(\mathbf{k})}\right|=\frac{1}{kT}\sum_{k=1}^{k}\ln\left|\boldsymbol{\delta}\mathbf{x}^{(\mathbf{k})}\right|. \tag{66}$$

3.7 FTLE

The relaxation of both limits in the definition Eq. (50) leads to the notion of a finite-time Lyapunov exponent (FTLE), which is the finite-time average of the maximum expansion or contraction rate for pairs of passively advected fluid particles. More specifically, FTLE is defined as

$$\sigma_{t_0}^{t}\left(\mathbf{x}_0\right) = \frac{1}{2\left(t-t_0\right)} \ln \lambda_{max}\left(t, t_0, \mathbf{x}_0\right) \tag{67}$$

where $\lambda_{max}\left(t, t_0, \mathbf{x}_0\right)$ is the eigenvalue of the deformation-gradient tensor field (also known as a Cauchy-Green strain tensor) $\Sigma_t\left(\mathbf{x}_0, t_0\right)$ which is defined by the following expression

$$\Sigma_t\left(\mathbf{x}_0, t_0\right) = \left[\frac{\partial \mathbf{x}\left(\mathbf{x}_0, t\right)}{\partial \mathbf{x}_0}\right]^T \left[\frac{\partial \mathbf{x}\left(\mathbf{x}_0, t\right)}{\partial \mathbf{x}_0}\right]. \tag{68}$$

FTLE $\sigma_{t_0}^{t}\left(\mathbf{x}_0\right)$, a finite-time generalization of Eq. (50), can be computed from finite-time velocity samples in real fluid flows with general time dependence.

3.8 Fractal properties of trajectories. Fractal dimension

Discrete samples $\{x\left(t_i\right), y\left(t_i\right)\}$, $i = 1, 2, \cdots$ of fluid particle trajectories, given by Eqs. (2), may exhibit fractal properties in nonsteady fluid flows, even in the case when the streamfunction $\psi\left(x, y, t\right)$ is specified analytically [43]. One of the most commonly exploited manifestations of fractal behavior of trajectories is anomalous diffusion, which is characterized by the root-mean-square growth of particle displacements proportional to $t^{1/FD}$ with fractal dimension $FD \epsilon [1, 2]$. Ballistic motion is characterized by $FD = 1$ and Brownian motion is characterized by $FD = 2$.

A box counting algorithm described below (see [43] for details) allows one to estimate the fractal dimension FD of trajectory from it's discrete sample $\{x(t_i), y(t_i)\}$, $i = 1, 2, \cdots, N$ in systems with a bounded phase space. The phase space of the system is first mapped onto a unit square and then by turns divided into 2^{2m}, $m = 0, 1, 2, \cdots$ square boxes. At the m-th step, the length of the box side is $s(m) = 2^{-m}$ and the area of the box is $s^2 = 2^{-2m}$. Probabilities $P_i(s)$ for a point from a discrete trajectory sample to occupy the i-th square are then computed. The scaling relationship

$$C(s) \equiv \sum_i [P_i(s)]^2 \approx s^{FD} \tag{69}$$

is then used to estimate the fractal dimension FD of the trajectory. Note that from the last equation it follows that $C(1) = 1$ (all points from the discrete trajectory sample fall into 1 box at the $m = 0$ step) and $\lim_{s \to 0} C(s) = \sum_{i=1}^{N} [1/N]^2 = 1/N$ (as the number of boxes $m \to \infty$, each point from the discrete trajectory sample occupies its own box).

3.9 KAM theorem

In the XIXth century, the study of integrable problems, such as the two-body problem or linear oscillations problem, was of the major interest. After the work of Poincare, however, it became clear that the general dynamical system in nonintegrable (i.e., its integrals of motion are not only unknown but do not exist).

All integrable problems with n degrees of freedom possess n single-valued first integrals of motion in involution. Thus, in the $2n$-dimensional phase space the motion occurs on invariant n-dimensional manifolds. If the phase space of the system is

bounded, these invariant manifolds are n-dimensional tori. A vivid example of such behavior is provided by 2-dimensional incompressible steady fluid flows with streamfunction $\psi = \psi_0(x, y)$ discussed in Sec. 3.1. Fluid particle trajectories in such flows, resulting from solving Eqs. (2), can be thought as either 1-dimensional surfaces in (x, y) or tori in higher-dimensional phase space.

When a steady fluid flow is subjected to a small time-dependent perturbation, many tori of the unperturbed system will break up and chaotic motion will occur. However, the survival of some nonchaotic trajectories (or tori) is predicted by the Kolmogorov-Arnold-Moser (KAM) theorem for certain classes of time-dependent perturbation. According to each of the many variants of the KAM theorem [44, 45, 46, 47], many of the unperturbed tori associated with the steady streamfunction survive under the perturbation provided certain conditions are met. Due to the strong KAM stability phenomenon [7], under most conditions, the invariant tori that are most likely to survive in the perturbed system are those in close proximity of the shearless or nontwist trajectory that is characterized by $\omega' = 0$.

The original Kolmogorov [44] form of the KAM theorem is suitable for 2D incompressible fluid flows with the streamfunction of the form

$$\psi(x, y, t) = \psi_0(x, y) + \epsilon\psi_1(x, y, \sigma t) \tag{70}$$

where ψ_1 is a periodic function in t with period $2\pi/\sigma$ and ϵ is the perturbation strength parameter. According to the theorem, tori in the vicinity of those tori of the unperturbed system for which the ratio $\omega(I)/\sigma$ is sufficiently irrational survive in the

perturbed system provided the strength of the perturbation is sufficiently weak and a nondegeneracy condition is satisfied. The condition of sufficient irrationality of the ratio $\omega(I)/\sigma$ is expressed quantitatively by means of a Diophantine condition. Its meaning is straightforward and will not be discussed further. The application of the nondegeneracy condition, on the other hand, is more challenging and will be discussed in more detail. In the simplest form of the theorem the nondegeneracy condition reads $\omega'(I) \neq 0$, which guarantees the invertibility of $\omega(I)$. This form of the nondegeneracy condition was used in Kolmogorov original statement of the theorem [44]. Already in the original proof of the theorem, Arnold [45] noted in the footnote that an alternative form of the nondegeneracy condition, an isoenergetic condition, could be used instead. Subsequently, Bruno [48], Russmann [46] and Sevryuk [47] announced forms of the theorem that employ less restrictive nondegeneracy conditions.

The significance of the Russmann nondegeneracy condition is that for the system of the form Eq. (70) it is satisfied in domains that include isolated zeros of $\omega'(I)$, i.e. that are degenerate in Kolmogorov sense. The Russmann nondegeneracy condition is most naturally stated in words: for an autonomous system with $N+1$ degrees of freedom the image of the frequency map $I \to \omega(I)$ may not lie on any hyperplane of dimension N that passes through the origin. Applying this condition to systems of the form Eq. (70) requires transforming the system into an equivalent autonomous 2 degree-of-freedom system with a bounded phase space. Such transformation is a special case of the transformation given at the end of this section. After performing this transformation, the Russmann nondegeneracy condition requires that in the (ω, σ)-space the locus of points $(\omega(I), \sigma)$ does not lie on a line that passes through

the origin. In other words, the Russmann nondegeneracy condition is satisfied in domains that include isolated zeros of $\omega'(I)$ and is only violated if $\omega(I) = \text{const}$. The Russmann form of the theorem is weaker that the original Kolmogorov's form because it only guarantees the existence of tori in the perturbed system whose frequencies are close to those in the unperturbed system, but it does not guarantee that a torus with a particular value of I will survive in the perturbed system with unchanged frequency. For our purposes this distinction is not important because we are interested in the presence of transport barriers and, from this point of view, it makes no difference whether a particular torus with a fixed value of I or rather some nearby tori survive in the perturbed system.

A version of the KAM theorem for quasiperiodically-perturbed one degree-of-freedom Hamiltonian systems that satisfy the Russmann nondegeneracy condition has been proven recently by Sevryuk [47]. This form of the KAM theorem is suitable for 2D incompressible fluid flows with the streamfunction of the form

$$\psi(x, y, t) = \psi_0(x, y) + \epsilon\psi_1(x, y, \sigma_1 t, \sigma_2 t, \cdots, \sigma_N t) \tag{71}$$

where ψ_1 is a multiperiodic function in t with constituent periods $2\pi/\sigma_i$, $i = 1, 2, \cdots, N$ and $\epsilon \ll 1$ is the perturbation strength.

An important observation relating to systems of the form (71) is that only frequencies that are incommensurable (i.e., have the property that the ratio of all pairs of frequencies is irrational) need to be considered. Otherwise, if we consider, for example, a multiperiodic function with periods 4 and 6 days, the resulting function is a

simple periodic function with period 12 days. In general, a reduction of the number of frequencies can be achieved whenever two or more of the frequencies are commensurable. Thus, without loss of generality, it may be assumed that $\sigma_1, \sigma_2, \ldots, \sigma_N$ are incommensurable, i.e., that ψ_1 is a quasiperiodic with N incommensurable frequencies.

Recall from Sec. 3.2 that for periodically-perturbed systems of the form Eq. (70) each surviving KAM torus is a 2D surface in the 3D space $(x, y, t \bmod 2\pi/\sigma)$ that divides the 3d space into nonintersecting "inside" and "outside" regions and thus provides an impenetrable barrier to transport. An extension of the same argument applies to the quasiperiodic problem. We show below that in quasiperiodically-perturbed systems of the form Eq. (71) each surviving KAM torus has the dimension one less than the dimension of space that the chaotic trajectories fill [43, 49]. Thus, each surviving KAM torus provides an impenetrable barrier for transport.

To see this, note first that the nonautonomous 1 degree-of-freedom system described by equations (2) and (70) can be written as an equivalent autonomous $N+1$ degree-of-freedom system,

$$\frac{dq_i}{d\tau} = \frac{\partial H}{\partial p_i}, \quad \frac{dp_i}{d\tau} = -\frac{\partial H}{\partial q_i}, \quad i = 1, 2, \ldots, N+1 \tag{72}$$

where $q_i = \sigma_i t$, $p_i = -\psi/\sigma_i$, $i = 1, 2, \ldots, N$, and $q_{N+1} = y$, $p_{N+1} = x$, with

$$H(\mathbf{p}, \mathbf{q}) = \psi(p_{N+1}, q_{N+1}; q_1, q_2, \ldots, q_N) + \sum_{i=1}^{N} \sigma_i p_i. \tag{73}$$

It is straightforward to verify that (72) and (73) reduce to $dt/d\tau = 1$, equations (2) and $d\psi/dt = \partial\psi/\partial t$. An important property of the transformed system (72, 73) is that each trajectory is constrained by the presence of N integrals (sometimes called constants of the motion), i.e., N functions $f_i(\mathbf{p}, \mathbf{q})$, $i = 1, 2, \ldots, N$ for which $df_i/d\tau = 0$. These integrals are H and $f_i = q_i/\sigma_i - q_N/\sigma_N$, $i = 1, 2, \ldots, N-1$. If one additional independent integral can be found, the system (72, 73) can be solved by quadratures and is said to be integrable. (This should come as no surprise because the original system (2, 70) also lacks only one integral to render it integrable.) For our purposes, the principal significance of the N integrals is that, because of their presence, each trajectory in the $2(N+1)$-dimensional phase space, lies on a surface of dimension $2(N+1) - N = N+2$. In a near-integrable system of this type in which both KAM tori and chaotic trajectories are present, the tori have dimension equal to the number of degrees of freedom, $N+1$. In the $N+2$-dimensional space that is filled by chaotic trajectories, the $N+1$-dimensional KAM tori serve as impenetrable transport barriers. (Note, for example, that in (x, y, z) the 1-d circle $x^2+y^2 = 1, z = 0$ divides the 2-d $z = 0$ plane into nonintersecting inside and outside regions, but the same 1-d circle does not divide the 3-d (x, y, z) volume into nonintersecting inside and outside regions.)

The argument just given shows that in the system described by (2) and (70) (or equivalently by (72) and (73)) Arnold diffusion does not occur. Loosely speaking, this is the process which allows chaotic trajectories to bypass KAM invariant tori. This process occurs in near-integrable autonomous systems with $N \geq 3$ degrees of freedom which, under perturbation, are constrained by only one integral H. For

such systems phase space has dimension $2N$, chaotic trajectories lie on surfaces of dimension $2N-1$, while KAM invariant tori have dimension N; for $N \geq 3$ these tori do not serve as impenetrable barriers to the chaotic trajectories. The cause of the absence of Arnold diffusion in the system described by (72) and (73) is the integrals in addition to H that constrain the motion of all trajectories.

3.10 Resonance widths and the "strong KAM stability" phenomenon

Hamiltonian systems that locally violate the twist condition ($\omega'(I) \neq 0$) arise in many applications, including simple mechanical systems [50], charged particle dynamics in magnetic fields [51], celestial dynamics [52], stellar pulsations [53], plasma physics [54], underwater acoustics [55], and transport and mixing in the ocean and atmosphere [49, 56]. Numerical simulations reveal that when systems of this type are perturbed, the degenerate or nontwist tori are remarkably stable. We refer to this phenomenon as "strong KAM stability" near degenerate tori. In this section we show that, owing to small resonance widths near degenerate tori under perturbation, robust transport barriers are found near such tori under typical conditions. The resulting transport barriers are important in all of the applications mentioned.

We consider a Hamiltonian system

$$\dot{I} = -\partial H/\partial\theta,\ \dot{\theta} = \partial H/\partial I \tag{74}$$

with Hamiltonian of the form

$$H\left(I,\theta,t\right)=H_0\left(I\right)+\epsilon H_1\left(I,\theta,\overrightarrow{\sigma}t\right), \tag{75}$$

where (I,θ) are action-angle variables, $\overrightarrow{\sigma}=\{\sigma_1,\cdots,\sigma_N\}$, H_1 is multiperiodic in time with periods $2\pi/\sigma_i$, $i=1,\cdots,N$ and ϵ is the strength of the perturbation. Without loss of generality, we may assume that frequencies $\sigma_1,\cdots,\sigma_N$ are incommensurable, otherwise a reduction of number of frequencies can be achieved. In the $\epsilon=0$ limit, Eqs. (74, 75) define motion on a torus (see Sec. 3.1 for details). As the strength of the perturbation ε becomes nonzero, many of the tori of the unperturbed system will break up under the influence of the perturbation. Torus destruction is caused by the excitation of resonances when the ratio of the frequency of the motion on the unperturbed torus, $\omega\left(I\right)$, to the forcing frequency, σ, is rational. Associated with each resonance is a characteristic width. Resonance widths are important because overlapping resonances lead to the destruction of the unperturbed tori with I-values between those of the resonant tori [57, 58, 59]. A general expression for the width of a resonance is derived below. It will be shown that resonance widths scale like $\Delta\omega\sim\varepsilon^{j/(j+1)}$ where $j=1,2,3,\ldots$ is the number of nondegenerate resonances that coalesce at the degenerate point (the case of the nondegenerate resonance corresponds to $j=1$). We refer to j below as the order of the degeneracy. For small ε degenerate resonance widths are generally smaller than nondegenerate resonant widths. This leads to the phenomenon of "strong KAM stability" and very robust transport barriers near degenerate tori. An example will be given below.

We start the derivation of a general expression for the width of a resonance by noting that since the perturbation H_1 is multiperiodic in time and 2π periodic in θ, it can be expanded into Fourier series

$$H_1(I,\theta,t) = \sum_{\overrightarrow{m},n=-\infty}^{\infty} V_{nm}(I)\cos\left(n\theta - \overrightarrow{m}\,\overrightarrow{\sigma}t + \phi_{n\overrightarrow{m}}\right) \tag{76}$$

where $\overrightarrow{m} = m_1, \cdots, m_N$ and $\phi_{n\overrightarrow{m}}$'s are phases. The equations of motion are

$$\dot{I} = \varepsilon \sum_{\overrightarrow{m},n=-\infty}^{\infty} nV_{n\overrightarrow{m}}(I)\sin\left(n\theta - \overrightarrow{m}\,\overrightarrow{\sigma}t + \phi_{n\overrightarrow{m}}\right), \tag{77}$$

$$\dot{\theta} = \omega(I) + \varepsilon \sum_{\overrightarrow{m},n=-\infty}^{\infty} nV'_{n\overrightarrow{m}}(I)\cos\left(n\theta - \overrightarrow{m}\,\overrightarrow{\sigma}t + \phi_{n\overrightarrow{m}}\right). \tag{78}$$

Let $\omega^{(j)}(I_0)$ denote the jth derivative of $\omega(I)$ at $I = I_0$. In the following we shall assume that ε is small, $\omega(I)$ satisfies $\omega^{(j-1)}(I_0) = 0$, $\omega^{(j)}(I_0) \neq 0$ for some integer $j \geq 2$ and some I_0 in the I-domain of interest, and $\overrightarrow{\sigma}$ is an adjustable N-dimensional parameter that is close to the value $\overrightarrow{\sigma}_0$ at which the resonance condition $n\omega(I_0) = \overrightarrow{m}\,\overrightarrow{\sigma}_0$ is satisfied. j is the number of nondegenerate resonances that coalesce at the degenerate point. Below j will be referred to as the order of the degeneracy.

In the approximate analysis that follows, we will consider the vicinity of the resonant level. Let $\psi = n\theta - \overrightarrow{m}\,\overrightarrow{\sigma}t + \phi_{n\overrightarrow{m}}$ be the term corresponding to the resonant set $\{n, \overrightarrow{m}\}$. Then $\dot{\psi} = n\dot{\theta} - \overrightarrow{m}\,\overrightarrow{\sigma}$. Following [58, 60], all the oscillating nonresonant terms in Eqs. (77) and (78) will be omitted, $V_{n\overrightarrow{m}}(I)$ will be replaced by the resonant value $V_{n\overrightarrow{m}}(I_0)$ and $\omega(I)$ will be expanded in a Taylor series about I_0 with $\delta I = I - I_0$.

For convenience, we introduce the notation $\Omega_i = \omega^{(i)}(I_0)/i!$, $i = 0, 1, \ldots, j-2$. The following approximate autonomous system results from Eqs. (77) and (78) in the vicinity of the resonant level:

$$\delta\dot{I} = \varepsilon n V_{n\overrightarrow{m}}(I_0)\sin\psi, \tag{79}$$

$$\dot{\psi} = n\left(\Omega_0 + \Omega_1\delta I + \ldots + \Omega_{j-2}(\delta I)^{j-2} + \omega^{(j)}(I_0)\frac{(\delta I)^j}{j!}\right) - \overrightarrow{m}\,\overrightarrow{\sigma}. \tag{80}$$

An $O(\varepsilon)$ term in Eq. (80) has been omitted. The justification for this is that it will be shown below (Eq. (85)) that δI scales like $\varepsilon^{1/(j+1)}$. Equations (79) and (80) define a Hamiltonian system

$$\delta\dot{I} = -\partial\tilde{H}/\partial\psi, \quad \dot{\psi} = \partial\tilde{H}/\partial\delta I \tag{81}$$

with Hamiltonian

$$\tilde{H}(\delta I, \psi) = n\left(\Omega_0\delta I + \Omega_1\frac{(\delta I)^2}{2} + \ldots + \omega^{(j)}(I_0)\frac{(\delta I)^{j+1}}{(j+1)!}\right) - \overrightarrow{m}\,\overrightarrow{\sigma}\,\delta I + \varepsilon n V_{n\overrightarrow{m}}(I_0)\cos\psi. \tag{82}$$

Consistent with Eq. (82) is the expansion

$$\omega(\delta I; \mathbf{\Omega}) = \Omega_0 + \Omega_1\delta I + \ldots + \Omega_{j-2}(\delta I)^{j-2} + \omega^{(j)}(I_0)\frac{(\delta I)^j}{j!}. \tag{83}$$

Below we estimate the width of a degenerate resonance of order j. At such a resonance $\overrightarrow{\sigma} = \overrightarrow{\sigma_0}$ with $\overrightarrow{m}\overrightarrow{\sigma_0} = n\Omega_0$ and $\Omega_1 = \Omega_2 = \ldots = \Omega_{j-2} = 0$, so the Hamiltonian (82)

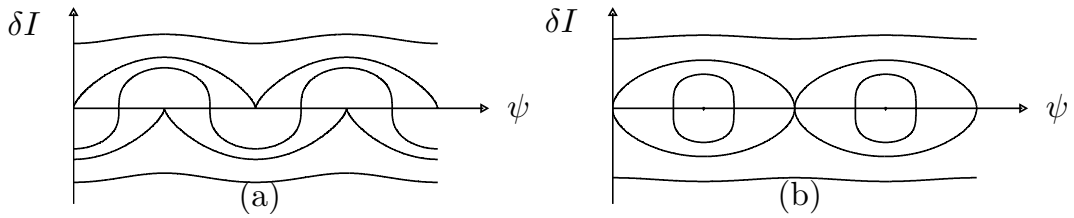

Figure 3: Level surfaces of $\tilde{H}(\delta I, \psi)$ defined by Eq. (84) in the phase plane $(\psi, \delta I)$ for $j = 2$ (a) and $j = 3$ (b).

reduces to

$$\tilde{H}(\delta I, \psi) = n\omega^{(j)}(I_0)\frac{(\delta I)^{j+1}}{(j+1)!} + \varepsilon n V_{n\vec{m}}(I_0)\cos\psi. \tag{84}$$

Level surfaces of $\tilde{H}$ in the phase plane $(\delta I, \psi)$ have qualitatively different features depending on whether j is odd or even. An example of each type is shown in Fig. 3. In both cases, however, trajectories are divided by a separatrix into two types: trajectories trapped in the resonance region and trajectories external to the resonance region. It is natural to define the resonance width as the width of the trapped region. This is the maximum δI excursion of the separatrix,

$$\Delta I = \left(\frac{2\varepsilon\left|V_{n\vec{m}}(I_0)\right|(j+1)!}{\left|\omega^{(j)}(I_0)\right|}\right)^{\frac{1}{j+1}}. \tag{85}$$

The corresponding frequency width is

$$\begin{aligned}\Delta\omega &= \left|\omega^{(j)}(I_0)\right|\frac{(\Delta I)^j}{j!} \\ &= \left|\omega^{(j)}(I_0)\right|^{\frac{1}{j+1}}\frac{\left(2\varepsilon\left|V_{n\vec{m}}(I_0)\right|(j+1)!\right)^{\frac{j}{j+1}}}{j!}.\end{aligned} \tag{86}$$

Equation (86) is the main result of this section.

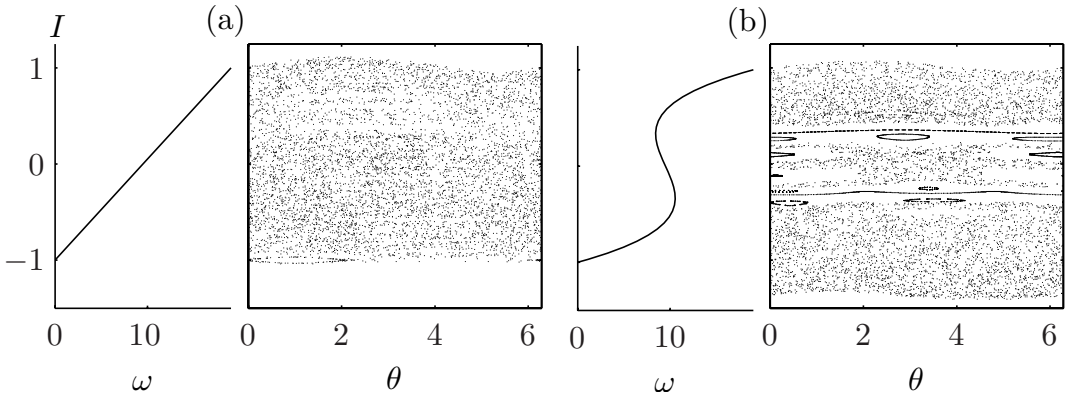

Figure 4: Frequency structure $\omega(I)$ and the corresponding Poincare section for the system with Hamiltonian $H_0(I) + \varepsilon H_1(I, \theta, \sigma t)$ for two choices of $H_0(I)$: (a) linear $\omega(I)$; (b) cubic $\omega(I)$. In both cases $\varepsilon = 0.026$ and $H_1(I, \theta, \sigma t) = \sum_{i=1}^{19} \cos(\sigma_i t) \cos(I + \theta)$, where the 19 forcing frequencies are commensurable and lie in the ω-domain plotted.

Because resonances are excited at discrete values of ω, it is the width $\Delta\omega$ rather than ΔI that determines whether neighboring resonances overlap. Note, that Eq. (86) applies as well to the nondegenerate case $j = 1$ providing that nondegenerate resonance widths scale like $\Delta\omega \sim (\epsilon |\omega'(I_0)|)^{1/2}$. Thus, small values of shear are generally associated with small resonance widths. Also from Eq. (86) it follows that degenerate resonances are generally associated with smaller resonance widths then nondegenerate resonances. As a result, resonances near degenerate tori are less likely to overlap and these regions are generally associated with enhanced stability. These arguments provide an explanation for the "strong KAM stability"phenomenon near degenerate tori, which is illustrated using $j = 2$ and $N = 1$ in Fig. 4. In that figure, Poincare sections for two systems with $H(I, \theta, t) = H_0(I) + \varepsilon H_1(I, \theta, \sigma t)$ are shown. The structure and strength of the perturbation term $\varepsilon H_1(I, \theta, \sigma t)$ is the same in both cases, but $H_0(I)$ is not. In one case $\omega(I)$ is linear. In the other case $\omega(I)$ is cubic and there are two isolated $j = 2$ degeneracies. The same $\omega(I)$-domain is present

for both choices of $H_0(I)$, so the same resonances are excited in both cases. The resonance widths are different, however, and, consistent with Eq. (86), this leads to strong stability of the tori in the vicinity of the degenerate tori in the system with cubic $\omega(I)$.

3.11 LCS

Theoretical work on dynamical systems [1, 2, 3, 4, 61] has characterized transport barriers in unsteady 2D incompressible flows as Lagrangian Coherent Structures (LCS). In such flows, transport barriers of two types are present. The first type is associated with invariant stable and unstable manifolds of generally nonstationary hyperbolic points. Barriers of this type are found in regions of chaotic motion. The second type corresponds to surviving KAM invariant tori and is associated with regular (nonchaotic) motion. Barriers of the second type are often found near cores of jet-like structures in the flow of interest and owe their existence to the strong KAM stability phenomenon. Because both invariant manifolds of nonstationary hyperbolic points and KAM tori are material lines of fluid, they provide impenetrable barriers for transport of passive tracers. The underlying dynamics is, however, completely different in the two cases.

Extracting LCS from measured or simulated velocity fields has proven to be a challenging task. As a first attempt, one may try to localize LCS from instantaneous streamline configuration. The main shortcoming of such approach is its frame-dependence, i.e. the location of features such as stagnation points depends highly on the coordinate system in which the velocity field is viewed. A frame-independent

approach to identifying LCS was developed in [1, 2, 3, 4]. It allows the partition of the phase space into elliptic, parabolic and hyperbolic regions, $E(t)$, $P(t)$ and $H(t)$, based on the sign of the inner product $\langle \xi^{\pm}, \mathbf{M}\xi^{\pm} \rangle$. Here vectors $\xi^{\pm}$ span the zero-strain set (define directions of zero strain), $\mathbf{M} = \dot{\mathbf{S}} + 2\mathbf{S}\nabla\mathbf{v}$ and $\mathbf{S}(\mathbf{x}, t)$ is the rate of strain tensor (the symmetric part of the velocity gradient field $\nabla\mathbf{v}(\mathbf{x}, t)$). LCS are then defined as locally the most robust hyperbolic, elliptic and parabolic material lines. Hyperbolic LCS, which attract or repel trajectories for locally the longest time in the flow, approximate stable and unstable manifolds of nonstationary hyperbolic points, respectively.

Another technique that is capable of detecting LCS involves computation of FTLEs. This Lyapunov-exponent-based detection scheme [4, 61, 62] is based on the notion that since hyperbolic LCS attract or repel trajectories for locally the longest time in the flow, the net growth of a unit vector transverse to them should be locally the largest. Consider a repelling structure $c(t)$ and select a unit vector $\mathbf{e}(t_0)$ at a point $\mathbf{x}_0(t_0) \in c(t_0)$ that is not tangent to $c(t_0)$. We propagate the unit vector along the trajectory $\mathbf{x}(t; \mathbf{x}_0, t_0)$ using the linearized flow map $\nabla_{\mathbf{x}_0}\mathbf{x}(t; \mathbf{x}_0, t_0)$ to obtain the evolution of the unit vector in time, $e(t) = \nabla_{\mathbf{x}_0}\mathbf{x}(t; \mathbf{x}_0, t_0)\, e(t_0)$. We now seek to maximize $|e(t)|$ over all possible choices of $\mathbf{x}_0$ and $e(t_0)$, i.e. we seek

$$\max_{|e|=1} |\nabla_{x_0} x(t; x_0, t_0)\, e(t_0)|. \tag{87}$$

For any matrix A, the following norm operator can be defined

$$\|A\| = \max_{|\mathbf{x}|=1} |A\mathbf{x}| = \sqrt{\nu_{max}\left(A^T A\right)}, \tag{88}$$

where $\nu_{max}\left(A^T A\right)$ is the largest eigenvalue of the positive definite symmetric matrix $A^T A$. With use of the definition Eq. (88), Eq. (87) becomes

$$\begin{aligned} &\max_{|e|=1} |\nabla_{\mathbf{x}_0}\mathbf{x}\left(t;\mathbf{x}_0,t_0\right) e\left(t_0\right)| = \|\nabla_{\mathbf{x}_0}\mathbf{x}\left(t;\mathbf{x}_0,t_0\right)\| \\ &= \sqrt{\nu_{max}\left([\nabla_{\mathbf{x}_0}\mathbf{x}\left(t;\mathbf{x}_0,t_0\right)]^T[\nabla_{\mathbf{x}_0}\mathbf{x}\left(t;\mathbf{x}_0,t_0\right)]\right)}. \end{aligned} \tag{89}$$

Comparing the last expression Eq. (89) with the FTLE definition Eq. (67) reveals that repelling (attracting) LCS correspond to maximizing curves or ridges of FTLE field computed in forward (backward) time (see [61, 62] for more detail). The FTLE-based detection scheme is also capable of detecting barriers of the second type, which are linked to surviving KAM invariant tori. Barriers of this type are associated with regular motion and thus are characterized by generally narrow bands of anomalously small values of FTLE.

4 Stratospheric Polar Vortex

The work reported in this chapter was motivated by a desire to understand the mechanism by which ozone-depleted air is trapped within the ozone hole. In that problem the atmospheric flow is assumed to be two-dimensional and incompressible; fluid particle trajectory equations then have Hamiltonian form. In the austral winter and early spring, winds at high latitudes in the stratosphere are characterized by a nearly zonal eastward jet. In this section it is shown that owing to the "strong KAM stability" phenomenon, invariant tori near the core of the zonal jet provide a robust barrier to meridional transport of passive tracers under commonly encountered conditions. Causes for the breakdown of such a barrier are discussed.

This chapter is organized as follows. In Sec. 4.1 a dynamically motivated simple analytical form of the streamfunction is derived, which is known as a Bickley jet. It consists of a zonal jet background flow on which two traveling Rossby waves are superimposed. In a reference frame moving with one of the Rossby waves, the flow consists of a steady background subject to a time-periodic perturbation. In Sec. 4.2 the Lagrangian dynamics in such a system is discussed with the emphasis on the "strong KAM stability" of tori near the core of the zonal jet. It is shown that, under typical conditions, trajectories near the core of a zonal jet provide a barrier to the meridional transport. In Sec. 4.3 a more general system is considered, which consists of a steady zonal flow subject to a time-multiperiodic perturbation. It is argued that conclusions of the previous subsection are unchanged in the time-multiperiodic case. In Sec. 4.4 our "strong KAM stability" argument for the transport barrier at the

perimeter of the ozone hole is contrasted to the potential vorticity barrier argument.

4.1 Bickley Jet

The ozone hole forms in the stratosphere over Antarctica in the austral late winter/early spring as a result of a sequence of chemical reactions whose initiation requires the right combination of low temperatures and light. Some depletion of ozone also occurs over the Arctic in the northern hemisphere late winter/early spring, but this is generally less severe than its Antarctic counterpart and the trapping mechanism described below is less efficient. In the winter and early spring, winds at high latitudes in the stratosphere are characterized by a nearly zonal eastward jet; the Stratospheric Polar Vortex (SPV) can be defined as the region poleward of the jet core. With this system in mind, we consider the Lagrangian dynamics of zonal jets in the atmosphere, with particular attention paid to explaining why, under commonly encountered conditions, zonal jets serve as barriers to meridional transport.

With a focus on the zonal jet, it is natural to make use of a β-plane approximation with $\beta = (2\Omega/r_e)\cos\varphi_0$ defined at the latitude φ_0 of the core of the zonal jet. Here $\Omega = 2\pi/\left(1\text{day}\right)$ is the angular frequency of the Earth's rotation and $r_e = 6371$ km is the Earth's radius. We consider an incompressible two-dimensional flow on an isentropic surface in the atmosphere (or surface of constant potential density in the ocean), which allows the introduction of streamfunction $\psi\left(x, y, t\right)$, where x increases to the east from an arbitrarily chosen longitude and y increases to the north from φ_0. The fluid parcel trajectory equations of motion then have Hamiltonian form with the

streamfunction playing the role of the Hamiltonian ($\psi(x,y,t) \leftrightarrow H(p,q,t)$),

$$\frac{dx}{dt} = -\frac{\partial\psi}{\partial y},\ \frac{dy}{dt} = \frac{\partial\psi}{\partial x}. \tag{90}$$

The streamfunction is dynamically constained. Consistent with our assumption of 2-d incompressible flow on a β-plane, conservation of potential vorticity $Q = \nabla^2\psi + \beta y$ dictates that

$$\frac{\partial Q}{\partial t} - \frac{\partial\psi}{\partial y}\frac{\partial Q}{\partial x} + \frac{\partial\psi}{\partial x}\frac{\partial Q}{\partial y} = 0. \tag{91}$$

A dynamically motivated model of a streamfunction, which is known as a Bickley jet, can be derived by assuming

$$\psi(x,y,t) = \psi_0(y) + \psi_1(x,y,t), \tag{92}$$

where ψ_1 will be treated as a small perturbation to ψ_0. The same streamfunction has been used previously in [56], and [63]. Our presentation follows that of del-Castillo-Negrete and Morrison; more details can be found in that work. Substituting Eq. (92) into Eq. (91) and keeping only leading-order terms yields

$$\frac{\partial}{\partial t}\nabla^2\psi_1 + u_0(y)\frac{\partial}{\partial x}\nabla^2\psi_1 + (\beta - u_0''(y))\frac{\partial\psi_1}{\partial x} = 0, \tag{93}$$

where prime denotes a differentiation with respect to y. Further, assuming that $\psi_1 = \phi(y)\exp(ik(x-ct))$, the last equation yields the Reyleigh-Kuo equation

$$(u_0(y) - c)(\phi''(y) - k^2\phi(y)) + (\beta - u_0''(y))\phi(y) = 0. \tag{94}$$

The Bickley jet velocity profile is a zonal jet that has a single maximum at $y = 0$ and is given by [64]

$$u_0(y) = U_0 \mathrm{sech}^2\left(\frac{y}{L}\right), \tag{95}$$

where U_0 and L are constants. For this velocity profile, Eq. (94) admits two neutrally stable ($\mathrm{Im}c = 0$) solutions of the form

$$\phi_i(y) = A_i U_0 L \mathrm{sech}^2\left(\frac{y}{L}\right), \tag{96}$$

provided that

$$U_0 L^2 k^2 = 6c, \tag{97}$$

$$6c^2 - 4U_0 c + \beta U_0 L^2 = 0 \tag{98}$$

and

$$\beta L^2 / U_0 < 2/3. \tag{99}$$

Here A_i, $i = 1, 2$ are dimensionless amplitudes, β, U_0 and L are environmental parameters that define c and k through Eqs. (97) and (98). Because of the periodic boundary conditions in x, at $\phi_0 = 60^\circ$ only the following discrete set of k is allowed

$$k_n = \frac{2n}{r_e}, \quad n = 1, 2, \ldots. \tag{100}$$

For numerical simulations we have chosen the following values of the parameters: $U_0 = 62.66$ m/s, $L = 1770$ km, corresponding to zonal wavenumbers $n = 2$ and $n = 3$, $c_2/U_0 = 0.205$ and $c_3/U_0 = 0.461$. This choice is self-consistent and satisfies

Eqs. (97), (98) and (100) simultaneously. The streamfunction is then

$$\psi(x,y,t) = -U_0 L \tanh\left(\frac{y}{L}\right) + A_3 U_0 L \operatorname{sech}^2\left(\frac{y}{L}\right)\cos(k_3(x-c_3t)) + A_2 U_0 L \operatorname{sech}^2\left(\frac{y}{L}\right)\cos(k_2(x-c_2t)). \quad (101)$$

An important observation is that the time dependence associated with one of the two Rossby waves in (101) can be eliminated by viewing the flow in a reference frame moving at the phase speed of that wave. In the reference frame moving at speed c_3 the streamfunction is

$$\psi(x,y,t) = c_3 y - U_0 L \tanh\left(\frac{y}{L}\right) + A_3 U_0 L \operatorname{sech}^2\left(\frac{y}{L}\right)\cos(k_3 x) + A_2 U_0 L \operatorname{sech}^2\left(\frac{y}{L}\right)\cos(k_2 x - \sigma_2 t) \quad (102)$$

where $\sigma_2 = k_2(c_2 - c_3)$. Note that σ_2 is negative because in the reference frame moving at the faster $n = 3$ wave, the $n = 2$ wave has westward propagating phases. Thus, in a moving reference frame the motion is governed by the pair of Hamilton's equations with streamfunction Eq. (102) consisting of two parts, a steady background flow

$$\psi_0(x,y) = c_3 y - U_0 L \tanh\left(\frac{y}{L}\right) + A_3 U_0 L \operatorname{sech}^2\left(\frac{y}{L}\right)\cos(k_3 x) \quad (103)$$

and a time-periodic perturbation

$$\psi_1(x,y,\sigma_2 t) = A_2 U_0 L \operatorname{sech}^2\left(\frac{y}{L}\right)\cos\left(k_2 x - \sigma_2 t\right). \quad (104)$$

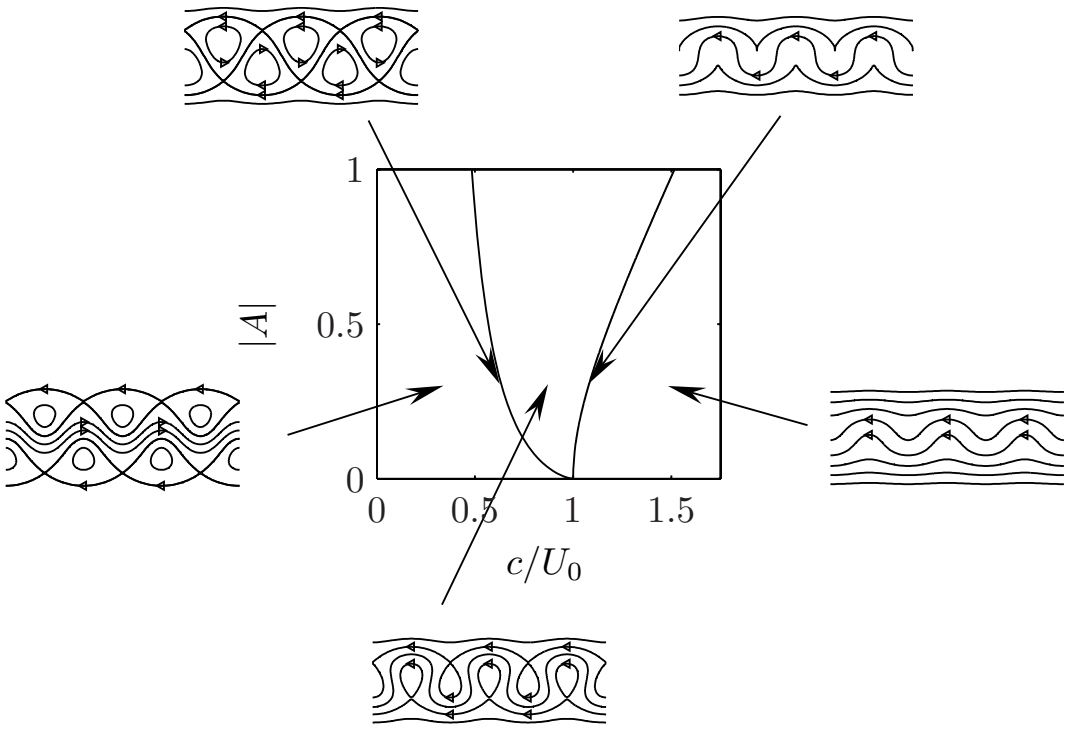

Figure 5: Bifurcation diagram in the $(A, c/U_0)$ parameter space corresponding to the streamfunction $\psi(x,y) = cy - U_0 L \tanh\left(\frac{y}{L}\right) + AU_0 L \mathrm{sech}^2\left(\frac{y}{L}\right)\cos(kx)$.

Nondimensionalization ($\psi \to \psi/(U_0 L), x \to kx, y \to y/L$) reveals that there are two irreducible dimensionless parameters, A_3 and c_3/U_0 that govern the structure of the background flow. A bifurcation diagram (Fig. 5) shows that there are 3 topologically distinct regions and two critical curves separating these regions. Depending on the choice of A_3 and c_3/U_0, the zonal jet may be strong, weak or absent. All possible topologies for ψ_0 can be revealed by holding $A_3 = \text{const}$ while varying c_3/U_0. For the SPV problem, the relevant domain on the bifurcation diagram is small values of both dimensionless parameters.

4.2 A steady background flow subject to a time-periodic perturbation

We turn our attention now to the periodically perturbed Hamiltonian systems (90) with streamfunction of the form

$$\psi(x, y, t) = \psi_0(x, y) + \psi_1(x, y, \sigma t), \tag{105}$$

of which Eq. (102) is a special case. The usual way to view trajectories in such system is to construct a Poincare section (see Sec. 3.2 for detail). Three examples, corresponding to the system described by Eq. (102) with $A_3 = 0.3$, $c_3/U_0 = 0.461$ and three choices of the perturbation strength A_2, are shown in Fig. 6. On these plots regular (nonchaotic) trajectories appear as discretely sampled smooth curves, while chaotic trajectories appear as sets of discrete samples that fill areas. The curves (corresponding to KAM invariant tori) that remain unbroken in the perturbed system represent impenetrable barriers to transport. From Fig. 6 it is seen that tori in the vicinity of the core of the zonal jet appear to be most resistant to breaking. This behavior is due to the "strong KAM stability" phenomenon described in Sec. 3.10; the connection will be explained below.

An additional Poincare section is shown in Fig. 7. The parameters used to construct that figure are identical to those used to construct the middle panel of Fig. 6 except that in Fig. 7 U_0 is decreased to 41.31 so that c_3/U_0 is increased to 0.7. (Note that with this change the flow is no longer a dynamically self-consistent Bickley jet.) This transition shows qualitatively what happens during the spring warming of the

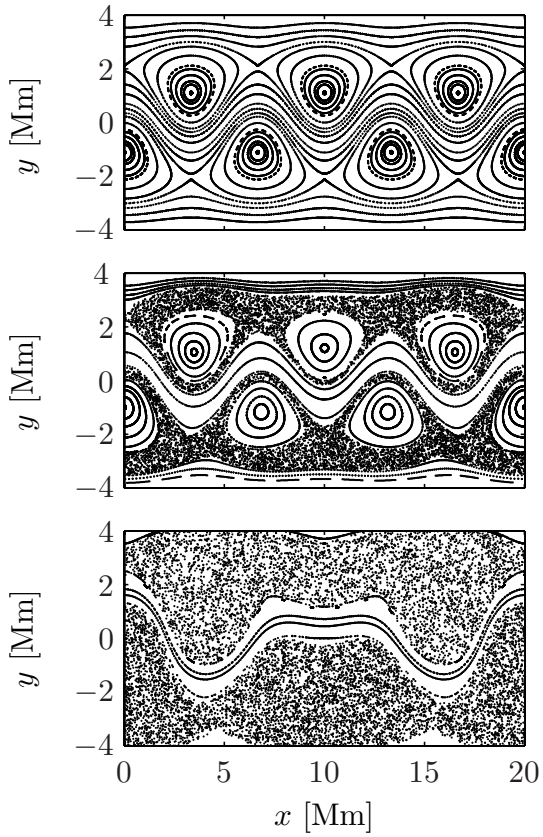

Figure 6: Poincare sections corresponding to the system described by equations (90) and (102) with $c_3/U_0 = 0.461$ and $A_3 = 0.3$ for three values of A_2: 0 (upper plot), 0.1 (middle plot), and 0.7 (lower plot). Note the robustness of the tori in the vicinity of the jet core.

polar vortex, which is associated with a decrease in U_0, and illustrates the importance of the background flow. The transition from Fig. 6 to Fig. 7 corresponds to a shift to the right in the bifurcation diagram shown in Fig. 5; the new choice of parameters corresponds to conditions in the central region of the bifurcation diagram, but very close to the bifurcation curve on the left. The loss of stability of the central region in Fig. 7 is caused by the change in the background flow topology seen in Fig. 5, and in particular, the lack of stability of motion in the vicinity of hyperbolic chains under perturbation. The transition from Fig. 6 (middle panel) to Fig. 7 is consistent with the work described in [65] which focuses on the breakdown of the transport barrier

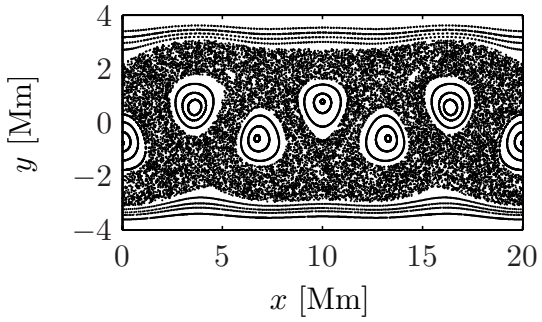

Figure 7: Poincare sections corresponding to the system described by equations (90) and (102) with $c_3/U_0 = 0.70$, $A_3 = 0.3$ and $A_2 = 0.1$. Note that the central barrier seen in the middle plot in Fig. 6 has been lost as a result of an increase in c_3/U_0.

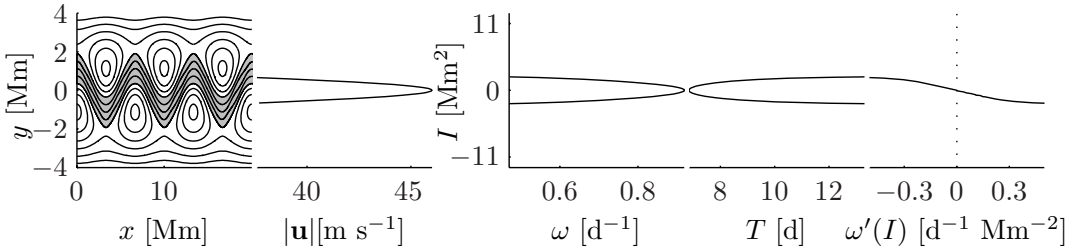

Figure 8: For the streamfunction $\psi_0(x, y)$ given by Eq. (103) with $A_3 = 0.3$, $c_3/U_0 = 0.461$: (a) selected level surfaces of $\psi(x, y)$; (b) $|\mathbf{u}|(y)$ at $k_3 x = \pi/2$; (c) $\omega(I)$; d) $T(I)$; and (e) $\omega'(I)$. In (b), (c), (d) and (e) only values of y and I corresponding to the shaded region near the jet core in (a) are shown.

at the perimeter of the polar vortex when c/U_0 exceeds a threshold that is close to unity.

In order to explain why the "strong KAM stability" transport barrier mechanism (recall Sec. 3.10) is relevant to tori in vicinity of the core of the zonal jet, we need to make use of action-angle variables (I, θ), which are introduced in the background flow $\psi_0(x, y)$. A canonical transformation $(x, y) \to (I, \theta)$ that transforms $\psi_0(x, y)$ to $H_0(I)$ is explained in Sec. 3.1 and is given by Eqs. (45) and (46). In the transformed system the equations of motion are $\dot{I} = -\partial H_0/\partial\theta = 0$, $\dot{\theta} = \partial H_0/\partial I \equiv \omega(I)$; I is a trajectory label and $T(I) = 2\pi/\omega(I)$ is the period of the motion, i.e., the time taken

by a trajectory to make one circle around the Earth.

For $A = 0.3$, $c/U_0 = 0.461$, plots of $|\mathbf{u}| = (u^2 + v^2)^{1/2}$, $\omega(I)$, $T(I)$ and $\omega'(I)$ are shown in Fig. 8 for trajectories in the vicinity of the jet core only. Note that from Fig. 3 it is seen that in the vicinity of the jet core $T(I)$ has a local minimum, $\omega(I)$ has a local maximum and $\omega'(I) = 0$. Thus, at the core of a jet there is a shearless torus, which corresponds to the degeneracy of order $j = 2$ ($\omega' = 0, \omega''(I) \neq 0$). This feature provides a basis for the "strong KAM stability" of tori in vicinity of the core of the zonal jet.

A simple analysis described in Sec. 3.10 reveals that nondegenerate resonance widths scale like $\Delta\omega \sim (\epsilon|\omega'(I)|)^{1/2}$. Thus, small values of shear $\omega'(I)$ are associated with small resonance width. The resonance width for a degenerate resonance of second order scales like $\Delta\omega \sim \epsilon^{2/3}|\omega'^{(I)|^{1/3}}$. Thus, for small ϵ the degenerate resonance width is generally smaller than the width of a nondegenerate resonance. Consequently, even though some resonances are excited near the jet core, the corresponding resonance widths are generally sufficiently small that neighboring resonances do not overlap. This provides a basis for the notion of "strong KAM stability" and explains the remarkable stability of the tori in the vicinity of the jet core. The stability of tori near the jet core is not absolute as the excitation of low-order resonance very close to the jet core can overcome the smallness of shear and change the picture.

4.3 A steady background flow subject to a time-multiperiodic perturbation

In this subsection we consider a simple generalization of Eq. (102), which consists of a multiperiodic perturbation superimposed on a steady background flow. An

important observation is that only frequencies that are incommensurable need to be considered, otherwise a reduction of number of frequencies can be made (see Sec. 3.9 for more details). Because all the mathematical difficulties associated with a multiperiodic perturbation are present already in the 2-frequency case and because this case is most convenient for numerical purposes, it is natural to focus on this case. Considered the streamfunction

$$\begin{aligned}\psi(x,y,t) &= c_3 y - U_0 L \tanh\left(\frac{y}{L}\right) + A_3 U_0 L \operatorname{sech}^2\left(\frac{y}{L}\right)\cos(k_3 x) \\ &\quad + A_2 U_0 L \operatorname{sech}^2\left(\frac{y}{L}\right)\cos(k_2 x - \sigma_2 t) + A_1 U_0 L \operatorname{sech}^2\left(\frac{y}{L}\right)\cos(k_1 x - \sigma_1 t).\end{aligned} \tag{106}$$

This streamfunction represents a steady zonal flow $\psi(y) = -U_0 L \tanh\left(\frac{y}{L}\right)$ on which a sum of three traveling Rossby-like waves is superimposed, viewed in a reference frame moving with speed c_3. The new perturbation term in Eq. (106) corresponds to zonal wavenumber 1 and, for convenience, is assumed to have the same meridional structure as other waves; the ratio σ_1/σ_2 is chosen here to be the golden mean $\left(\sqrt{5}-1\right)/2$, which is the most irrational real number. Unlike Eq. (102), the new multiperiodic streamfunction (106) is not dynamically motivated, but it is useful to illustrate some properties of quasiperiodic systems. In the $A_1 = 0$ limit Eq. (106) is identical to the streamfunction described by equation (102).

Since the background flow $\psi_0(x,y)$ has not changed and the analysis described in Secs. 3.9 and 3.10 apply to the time-multiperiodic perturbations, we expect that tori in the vicinity of the core of a zonal jet will exhibit "strong KAM stability" due to small resonance widths in this region. In Sec. 3.9 it was shown that, as in the

time-periodic case, in the time-multiperiodic case each surviving KAM invariant torus provides an impenetrable barrier to transport of passive tracers. With use of these two arguments, the conclusions of the previous section carry over to a time-multiperiodic perturbation. Under typical conditions, a thin band of surviving KAM invariant tori is expected to be present in the vicinity of the jet core that acts as a barrier to the meridional transport of passive tracers. The minor difference in behavior of the unbroken tori in time-multiperiodic case is that in the time-multiperiodic case these tori undulate with the same frequencies that are present in the perturbation. (For the time periodic case, the shape of the barrier repeats itself after each period of the perturbation.) For our purposes, this minor difference is not important because we are interested primarily in the presence or absence of the barrier.

Numerical simulations shown in Figs. 9, 10, and 11, which are based on the system defined by (106), serve to confirm our predictions. Figure 9 shows the time evolution of two sets of air parcels at times ranging from $t = 0$ to $t = 86$ days. The initial conditions are chosen to fall on two zonal lines $y = \text{const}$ on opposite sides of the zonal jet. It is seen that after 86 days each side of the jet is well stirred, as indicated by what appears to be random distributions of dots on each side of the jet, but there is no transport across a wavy boundary near the core of the jet. The cause of this behavior is a thin band of KAM invariant tori near the jet core that survive in the perturbed system and form a meridional transport barrier. This thin band of KAM invariant tori that separate the polar region from the midlatitude region in our idealized system undulates in a quasiperiodic fashion in time.

In Sec. 3.11 it was explained that FTLE-based detection scheme is capable of

identifying barriers to transport of two types: the first type is associated with stable and unstable manifolds of nonstationary hyperbolic points and the second type is associated with surviving KAM invariant tori. The latter type is often linked to the strong KAM stability phenomenon near shearless tori. Recall from Sec. 3.7 that the FTLE is a finite-time measure of the divergence rate of neighboring passively advected fluid particles. Because chaotic trajectories diverge at exponential rate and regular trajectories diverge at polynomial rate, regions of regular motion in the phase space are characterized by anomalously small values of FTLE. The distinction between chaotic and regular regions becomes more clear at longer integration times. In Fig. 10, FTLE is shown as a function of initial condition for a set of air parcel trajectories that spans the zonal jet. In the computation shown in Fig. 10, the integration time was chosen to be approximately 86 days. This figure shows that the region in the immediate vicinity of the jet core is characterized by thin band of anomalously small Lyapunov exponents, which indicates regular motion in this region. This is consistent with the interpretation that there is a narrow band of surviving KAM invariant tori in this region that provide a barrier to meridional transport.

For the same choice of parameters that was used to produce Figs. 9 and 10, the corresponding manifold structure is shown in Fig. 11. Two upper subplots of this figure show FTLE estimates, computed in backward time (upper subplot) and in forward time (middle subplot), as a function of initial condition for a set of air parcel trajectories that spans the zonal jet. The integration time used in this calculation was chosen to be approximately 1 week. In agreement with material presented in Sec. 3.11, regions of the most intense dark colors in the upper two subplots of Fig. 11,

which indicate maximizing ridges of FTLE estimates, correspond to stable and unstable manifolds of nonstationary hyperbolic points. In the lower subplot, segments of stable and unstable manifolds were produced with use of the double time-slice method described in Sec. 3.5. It requires evolving a set of initial conditions surrounding the hyperbolic point forward and backward in time during some integration interval. In the computations shown, a seeding procedure was implemented to produce smoothly resolved manifolds. We see from Fig. 11 that manifolds computed as maximizing ridges of the FTLE field agree with those computed with use of the double time-slice method. In the lower subplot of Fig. 11, segments of unstable manifolds are shown as red curves above the jet and pink curves below the jet; segments of stable manifolds are shown as blue and light blue curves. Lobe dynamics theory (see Sec. 3.3 for detail) predicts that in unsteady 2D incompressible fluid flows each nonstationary hyperbolic point is associated with a pair of stable and unstable manifolds. Intersecting stable and unstable manifolds produce lobes and govern transport of fluids in regions with chaotic behavior through the turnstile mechanism. In Figs. 9 and 10 it is seen that there are two nonintersecting regions associated with chaotic motion, which are separated from each other by a narrow band of regular motion. In agreement with Figs. 9 and 10, in Fig. 11 we see intersecting stable and unstable manifolds above the jet and intersecting stable and unstable manifolds below the jet. However, because chaotic regions above and below the jet are separated from each other by a thin band of regular motion near the core of the jet, intersections between invariant stable and unstable manifolds across the jet are prohibited (insuring that points from different

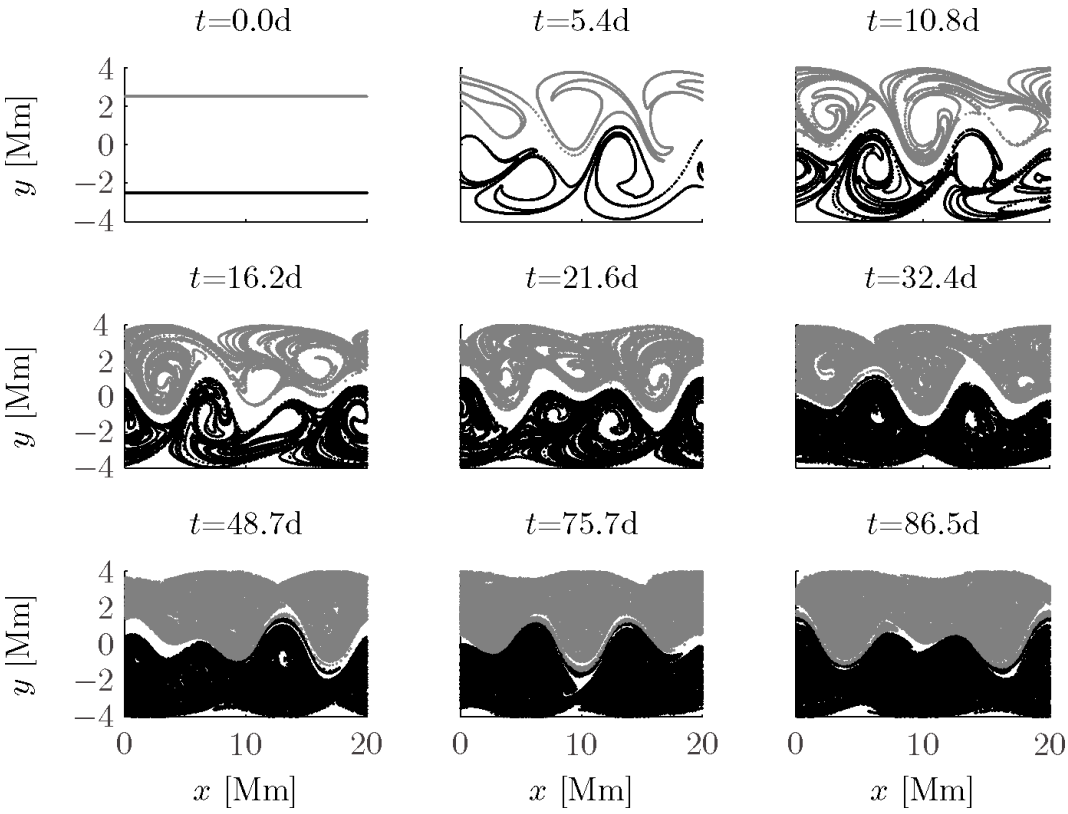

Figure 9: Time evolution of two sets of 25000 points that at $t = 0$ fall on zonal lines on opposite sides of the core of the zonal jet in the system described by equations (90) and (106) with $c_3/U_0 = 0.461$, $A_3 = 0.3$, $A_2 = 0.4$, $A_1 = 0.075$. Note that, although trajectories are predominantly chaotic, there is no transport across an undulating barrier in the vicinity of the jet core.

chaotic regions do not mix with each other).

In this subsection we have argued that, with some minor modifications, the conclusions of the previous section carry over to a multiperiodic perturbation. Numerical simulations provide strong evidence that such a result holds. The qualitative features that were described – the robust nature of nonchaotic trajectories near the jet core that serve to isolate chaotic trajectories on opposite sides of the jet – are expected to be seen whether there are 2 or 20 Rossby waves superimposed on the background zonal jet.

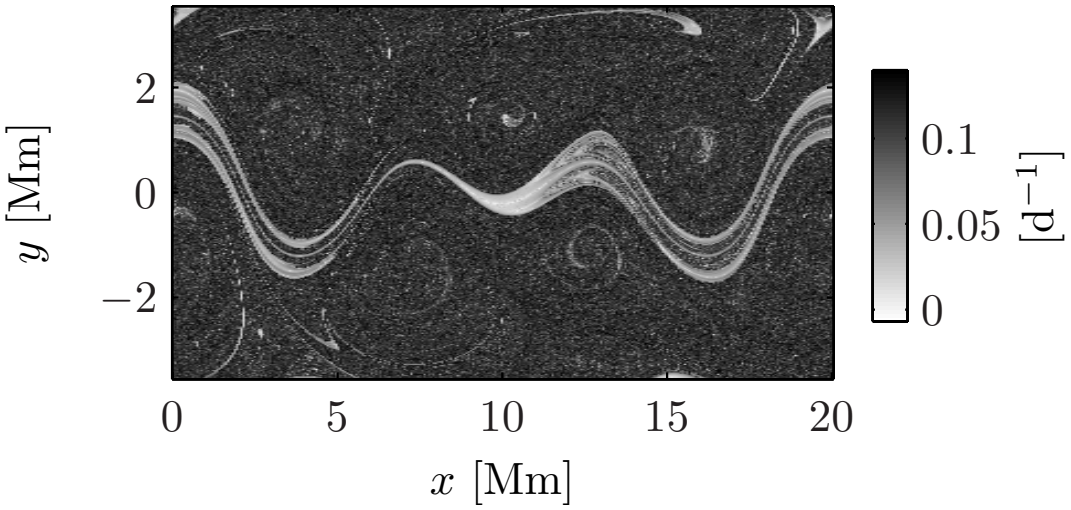

Figure 10: Finite-time Lyapunov exponent estimates as a function of initial position for the system described by equations (90) and (106) with $c_3/U_0 = 0.461$, $A_3 = 0.3$, $A_2 = 0.4$, $A_1 = 0.075$. The integration time for the estimates shown is 86.5 days. Note that the region in the vicinity of the jet core is characterized by small Lyapunov exponent estimates.

4.4 Connection to the potential vorticity barrier argument

In this subsection, a connection between our "strong KAM stability" explanation for the transport barrier at the perimeter of the ozone hole and "potential vorticity barrier" (PV-barrier or Q-barrier) explanation [66] (see also [67], [68] and references contained therein) of the transport barrier will be discussed.

A consequence of a nearly zonal transport barrier, like the one shown in Fig. 10, is that coarse-grained tracer distributions on opposite sides of the barrier are expected to be nearly homogeneous. This statement applies to both passive tracers and the dynamically active tracer Q. Thus associated with the transport barrier that we have described one expects to find a Q-barrier or Q-front.

According to the "potential vorticity barrier" explanation, the jump in Q across the perimeter of the polar vortex is the cause of the associated meridional transport

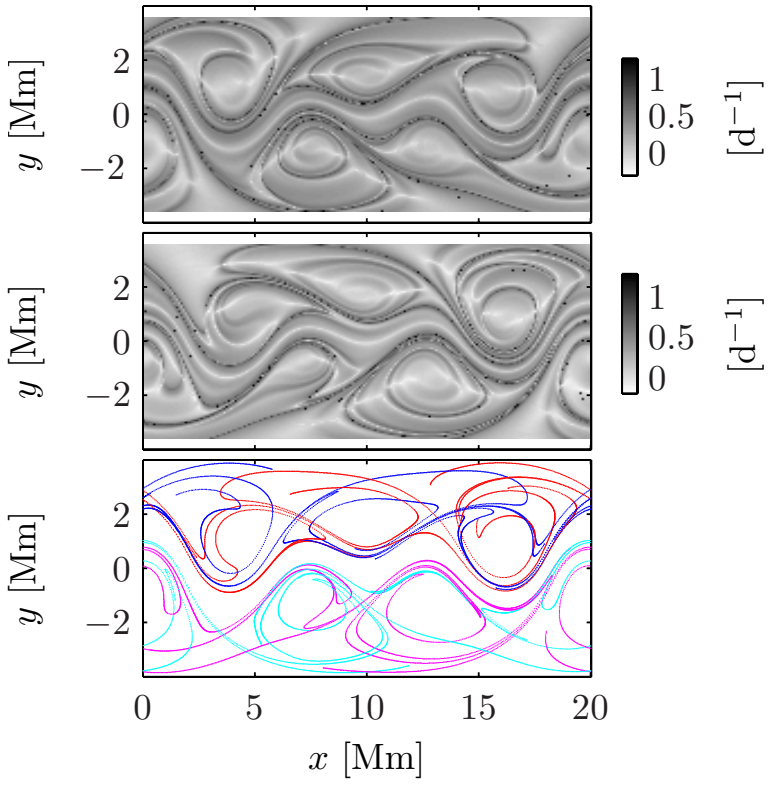

Figure 11: For the same model system that was used to produce Figs. 9 and 10, the corresponding stable and unstable manifold structure. Two upper subplots show FTLE estimates, computed in forward (upper subplot) and backward (middle subplot) time, as a function of initial condition for a set of air parcel trajectories that spans the zonal jet. The integration time for the estimates shown is 7 days. (lower subplot) segments of stable and unstable manifolds computed with use of the double time-slice method. Unstable manifolds are shown as red curves above the jet and pink curves below the jet; segments of stable manifolds are shown as blue and light blue curves, correspondingly, above and below the jet.

barrier. Associated with the jump in Q is a strong Q-gradient which, in turn, is associated with a strong Rossby wave restoring force and therefore a tendency to resist large scale deformation. The Rossby elasticity mechanism does not work at small scales, so it must be augmented by some other mechanism, which is shear, to explain the impermeability of the barrier to small-scale intrusions. The most recent discussion of these ideas is that of [68]. While we agree that a transport barrier at the perimeter of the ozone hole is associated with a jump in Q, we argue below

that it is most correct to think of the eastward zonal jet at the perimeter of the stratospheric polar vortex as being the cause of the barrier to meridional transport and the associated coarse-grained step in Q as a consequence of the transport barrier.

An interesting case to consider is the background flow

$$u\,(y) = u_0 + \beta y^2/2 \tag{107}$$

with $u_0 < 0$, corresponding to a westward zonal jet. Under perturbation, trajectories near the jet core will exhibit strong KAM stability and thus a robust meridional transport barrier near y = 0 is expected to be present. Moreover, under perturbation this flow is dynamically consistent in a coarse-grained sense with Q = const (the same value for positive and negative y). Note that to observe a transport barrier in this flow under perturbation, a tracer other than Q needs to be used. A dynamically consistent example of a barrier of this type was obtained numerically in [13]. This example shows that even in the absence of a Q-barrier, the strong KAM stability argument is valid. This strongly suggests that for eastward jets it is more natural to think of a jet as the cause (owing to strong KAM stability) of the barrier and the steplike Q-structure as a dynamically consistent consequence.

The role of shear will now be discussed. The quantity identified above as $\omega'(I)$ is a measure of shear. As noted above, nondegenerate resonance widths scale like $(\varepsilon|\omega'(I)|)^{1/2}$. Thus, as the magnitude of the shear $|\omega'(I)|$ increases, more resonances overlap and more tori – which would otherwise act as transport barriers – are broken. Shear is thus a destabilizing influence. This simple observation is consistent with the

arguments given above and our assertion that the *cause* of the transport barrier at the perimeter of the polar vortex is the eastward zonal jet at whose core is a shearless torus.

Some comments on the limits of validity of the analysis presented are appropriate. The most restrictive assumption is that the flow of interest consists of a time-multiperiodic perturbation superimposed on a steady background flow. The class of multiperiodic perturbations considered is surprisingly large. Recall that the number of terms N included in the multiperiodic perturbation need only be finite and that we focussed on the quasiperiodic case because this is the only mathematically nontrivial case to consider. Thus, with an appropriate choice of amplitudes and phases, the class of describable perturbations ranges from simple periodic ($N = 1$) to a deterministic wave packet (small N, narrow spectrum), to an approximation to white noise forcing (large N, flat and broad spectrum, random phases) – see, e.g., [69] for a discussion of the latter class of problems. Finally, we note that, although KAM theory assumes that the perturbation strength ε is small, numerical simulations show that invariant tori – and those in the vicinity of Kolmogorov-degenerate tori, in particular – persist for surprisingly large perturbation strengths. In the lower panel of Fig. 4, for instance, $\varepsilon = 0.7$. Thus the small ε assumption is less restrictive than one might expect.

5 Transport in a perturbed three-gyre system with application to the Adriatic Sea

Observations of surface drifters in the Adriatic Sea suggest the presence of a robust three-gyre background flow pattern. Motivated by this observation, surface transport in a three-gyre system is studied with the aid of dynamical systems techniques. The velocity field is assumed to be two-dimensional and incompressible. In this section, two models of the Adriatic Sea surface circulation are considered: 1) an observationally-based model of the Adriatic Sea consisting of the mean surface circulation derived from surface drifter trajectories on which a time-dependent altimetric perturbation velocity field is superimposed; and 2) an analytically prescribed model consisting of a steady three-gyre background on which a multiperiodic time-dependent perturbation is superimposed.

It is shown that the behavior of the perturbed three-gyre system undergoes an important qualitative change when the perturbation exceeds a certain threshold. For small perturbation, two nonoverlapping well-mixed figure-eight-shaped bands are present, each with a crossing region that includes a nonstationary hyperbolic stagnation point. These bands are separated from each other by a robust transport barrier. As a result, two of the gyres exchange no fluid with the third gyre. For large perturbation, one large well-mixed region is formed that includes portions of all three gyres. As a result, transport between all three gyres occurs. The qualitative change of behavior of the perturbed three-gyre system is accompanied by a corresponding qualitative change in its manifold structure. For a small perturbation, all stable and unstable manifold intersections are of the homoclinic type. When the perturbation

exceeds a certain threshold, heteroclinic intersections between stable and unstable manifolds are formed. In this section this behavior is described theoretically, illustrated using the analytically-prescribed model and shown to be consistent with the observationally-based model of the Adriatic.

This chapter is organized as follows. In Sec. 5.1 descriptive material on the Adriatic Sea is given: an observationally-based model of the mean surface circulation in the Adriatic Sea derived from surface drifter trajectories is described; and an idealized analytically prescribed three-gyre model of the mean surface circulation in the Adriatic Sea is introduced. In Sec. 5.2 numerical results based on the idealized three-gyre system subject to a multiperiodic perturbation are presented to illustrate the qualitative change in behavior of the perturbed three-gyre system as the perturbation strength increases. Relevant aspects of stable and unstable manifold structure, lobe dynamics, and KAM theory are discussed; the complementary nature of these ideas is emphasized. In Sec. 5.3 we turn our attention to a purely observationally-based model of the Adriatic Sea consisting of a surface-drifter-based estimate of the mean circulation on which a measured time-dependent altimetric perturbation is superimposed. It is demonstrated that all of the important qualitative features of the perturbed three-gyre model that were described in Sec. 5.2 can be identified in the observationally-based model. In Sec. 5.4 we summarize and discuss our results.

5.1 The Adriatic Sea mean surface circulation

The Adriatic Sea is the semi-enclosed elongated and somewhat rectangular basin of the Mediterranean Sea separating the Appenine peninsula from the Balkan region.

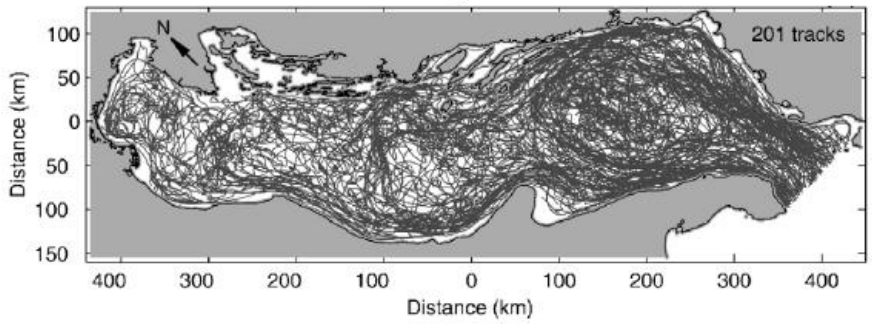

Figure 12: 201 surface drifter tracks in the Adriatic Sea between 1 August 1990 and 31 July 1999. (figure adapted from [28])

Its western coast is described by gentle curves, whereas its eastern coast has a more rugged coastline, including many islands. The circulation of the Adriatic Sea has been studied starting from the first half of nineteenth century so its qualitative characteristics are well known. A more quantitative knowledge of its mean surface circulation, transport and mixing properties is however more recent; previous studies of fluid motion in the Adriatic Sea are described in [70, 71, 27, 26, 72, 73, 74, 75, 28, 76, 77, 29].

A striking feature of the Adriatic Sea surface circulation is the robustness of the background multiple gyre flow pattern. Figure 12 (see also Fig. 1(b) in [28]) shows a large ensemble of surface drifter trajectories in the Adriatic Sea. The trajectories shown cover the period from August 1, 1990 to July 31, 1999. This plot gives insight into the mean surface circulation, its variability and the complexity of the associated Lagrangian motion. Neglecting the small northwesternmost gyre in the Adriatic basin (on the left side of the figure), three dominant gyres with cyclonic average circulation can be identified in Fig. 12. Drifters are seen to sometimes get trapped for a long time in one of the gyres, but many examples of drifters moving from one gyre to another can also be seen. These observations suggest the following question, which is

the central theme of this chapter: what controls intergyre transport in a perturbed three-gyre system?

In many of the previous studies of Lagrangian description of fluid motion in the Adriatic Sea ([26, 27, 28, 29]) a stochastic framework has been used. In this section we will make use of a dynamical systems approach. The flow is assumed to be two-dimensional and incompressible so that Eqs. (2) are valid. Furthermore, we shall assume that the streamfunction can be expressed as the sum of a steady background and a time-dependent perturbation,

$$\psi(x,y,t) = \psi_0(x,y) + \epsilon\psi_1(x,y,t), \tag{108}$$

where the dimensionless perturbation strength ϵ need not be small. It is natural to assume that the temporal mean of the perturbation is zero. The observational streamfunction $\psi_0(x,y)$ can then be estimated from time-averages of binned measured velocities. This can be done by writing a finite-difference approximation to the equations $\langle u\rangle = -\partial\psi_0/\partial y$, $\langle v\rangle = \partial\psi_0/\partial x$, followed by a least-squares fitting procedure. Figure 13 shows the result of such a calculation using surface-drifter-derived estimates of averaged velocities on a 0.1 deg grid using overlapping 0.2 deg $\times$ 0.2 deg bins.

In Fig. 13 the geographical domain of the Adriatic has been rotated counterclockwise by about 45° (as was done in Fig. 12) so that x increases from the northwest to the southeast. Also, for convenience the origin of the coordinate system has been shifted. To produce Fig. 13, the domain was closed by enforcing a no-flow condition

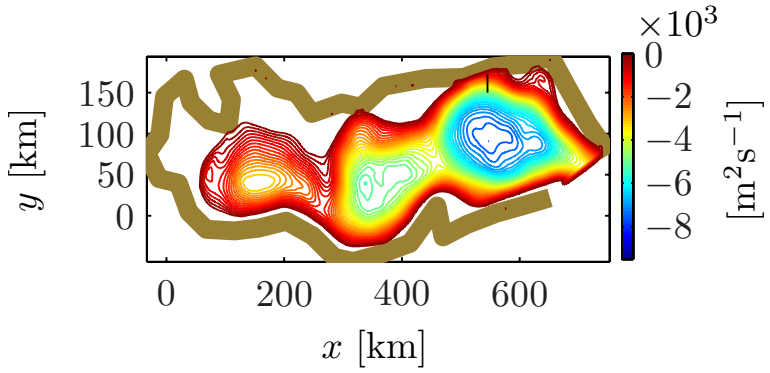

Figure 13: Level surfaces of the streamfunction $\psi_0(x,y)$ that describes the mean surface circulation in the Adriatic Sea inferred from surface drifter trajectories. The thick brown line shows the smoothed boundaries of the Adriatic basin. Black line at $x = 545$ km shows the initial positions of trajectories that were used to produce the left panel of Fig. 15.

through the Strait of Otranto (large x) and along coastlines. This smoothing of the boundaries does not affect the interior flow. The prominent three-gyre structure of the surface circulation, which is evident on Fig. 13, is consistent with the earlier discussion, based on Fig. 12. In subsection 5.3 a measured time-dependent altimetric perturbation will be added to this surface-drifter-based background streamfunction to obtain a fully observationally-based model of the Adriatic Sea surface circulation. Caveats relating to $\psi_0(x,y)$ shown in Fig. 13, including limitations linked to the relevance of a temporal mean circulation, will be discussed later.

We now introduce a simple analytically-prescribed background streamfunction $\psi_0(x,y)$:

$$\psi_0(x,y) = A\sin(Cy)\left(E-\cos(Bx)\right)\left(\exp\left(D\left(x-L_x\right)\right)-1\right)\left(x/L_x\right)^F. \qquad (109)$$

The values of the adjustable constants $L_x = 600$ km, $L_y = 150$ km, $A = 2.62\times10^3$ m^{2}s^{-1}, $B = 6\pi/L_x$, $C = \pi/L_y$, $D = 30/L_x$, $E = 3$ and $F = 1/2$ were chosen to mimic

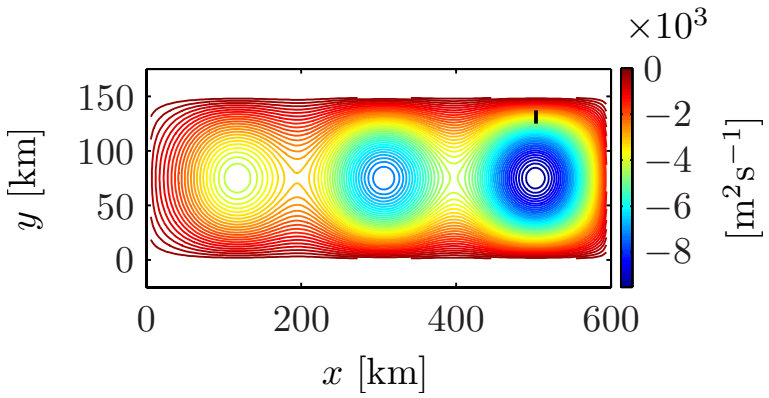

Figure 14: Level surfaces of the analytically-specified streamfunction $\psi_0(x, y)$ given by Eq. (109). Black line at $x = 500$ km shows the initial positions of simulated trajectories that were used to produce the right panel of Fig. 15.

the observationally-based streamfunction shown in Fig. 13. With these parameters, streamlines corresponding to Eq. (109) are shown in Fig. 14. Later in text, in subsection 5.2, this analytically specified background streamfunction will be subjected to a temporally multiperiodic perturbation to obtain an analytically-prescribed time-dependent model of the Adriatic Sea surface circulation. This analytical model will be used to illustrate the behavior of a perturbed three-gyre system as the perturbation strength increases. In spite of its simplicity, the analytically described background streamfunction Eq. (109) reproduces the three-gyre structure of the Adriatic Sea and has correct length and time scales as is evident from Figs. 14 and 15.

The background three-gyre geometry implies the existence of 5 stagnation points: 3 of the elliptic type that are associated with the core of each gyre and 2 of the hyperbolic type that separate adjacent gyres from each other. For the streamfunctions shown in Figs. 13 and 14, associated with each of the two hyperbolic stationary points is a homoclinic trajectory that goes through a stagnation point and is characterized by an infinitely long period of motion. The two homoclinic trajectories form two

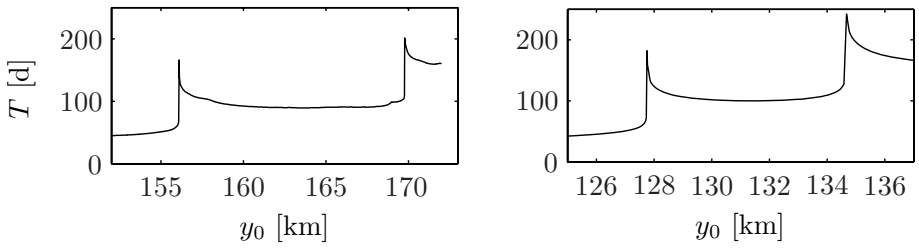

Figure 15: Periods of simulated trajectories, T, for a family of trajectories with variable initial position, y_0, obtained with use of: (left) observationally-based steady streamfunction that is shown in Fig. 13; (right) the analytically-specified steady streamfunction given by Eq. (109) that is shown in Fig. 14.

figure eights, one embedded inside the eastern loop of the other. The homoclinic trajectories separate regions of qualitatively different motion and are often referred to as separatrices. The special case in which the two hyperbolic stagnation points fall on the same level surface of ψ_0 has a different topology consisting of two heteroclinic and two homoclinic connections. That special case is not consistent with the observational data base (Figs. 12 and 13) and will not be considered here.

Fig. 15 shows periods of simulated trajectories, T, as a function of initial position for a set of trajectories that includes the two homoclinic trajectories. The left panel was constructed using the observationally-based streamfunction that is shown in Fig. 13.

The right panel of Fig. 15 was constructed using the analytically-specified streamfunction given by Eq. (109) that is shown in Fig. 14. The initial positions of the simulated trajectories that were used in these calculations are shown in Figs. 13 and 14, respectively, with black dots (at $x = 540$ km and $x = 500$ km, respectively). Three regions of qualitatively different motion can be identified on both panels of Fig. 15 based on the values of T in these regions: trajectories trapped inside the eastern gyre, trajectories going around the central and eastern gyre, and trajectories involved

in the basinwide motion, i.e. going around all three gyres. Homoclinic trajectories separate these three regions of qualitatively different motion from one another. Note that the initial positions y_0^h of the homoclinic trajectories coincide with the trajectories for which $T \to \infty$. Between the two homoclinic trajectories $T(y_0)$ has a local minimum. Note that the periods of simulated trajectories for our simple analytical streamfunction given by Eq. (109) are in good quantitative agreement with those produced by the streamfunction deduced from the drifter data.

We now review the essentials of action-angle variables as a first step towards applying some KAM-theory-related ideas. For any steady streamfunction $\psi_0(x, y)$ the Lagrangian equations of motion, Eq. (2), can be transformed to action-angle form: $(x, y) \to (I, \theta)$, $\psi_0(x, y) \to H(I)$. A canonical transformation $(x, y) \to (I, \theta)$ that transforms $\psi_0(x, y)$ to $H_0(I)$ is explained in Sec. 3.1 and is given by Eqs. (45) and (46). In the transformed system the equations of motion have the form Eq. (44), I is a trajectory label and motion is 2π-periodic in θ with angular frequency $\omega(I)$; the period of motion on a trajectory is $T(I) = 2\pi/\omega(I)$. Recall from Sec. 3.1 that the quantity $\omega'(I) = \mathrm{d}\omega/\mathrm{d}I$ is a measure of shear on a trajectory, and a trajectory satisfying the condition $\omega' = 0$ is referred to as shearless or twistless.

For the analytical streamfunction, Eq. (109), plots of $T(I)$, $\omega(I)$ and $\omega'(I)$ for trajectories lying between the two homoclinic trajectories are shown in Fig. 16. Note that in the vicinity of the homoclinic trajectories $T(I)$ and $\omega'(I)$ are large, while between the two homoclinic trajectories $T(I)$ has a local minimum, $\omega(I)$ has a local maximum and $\omega'(I) = 0$. In other words, between the two figure eights that are formed by homoclinic trajectories lies a shearless trajectory, while the vicinity of

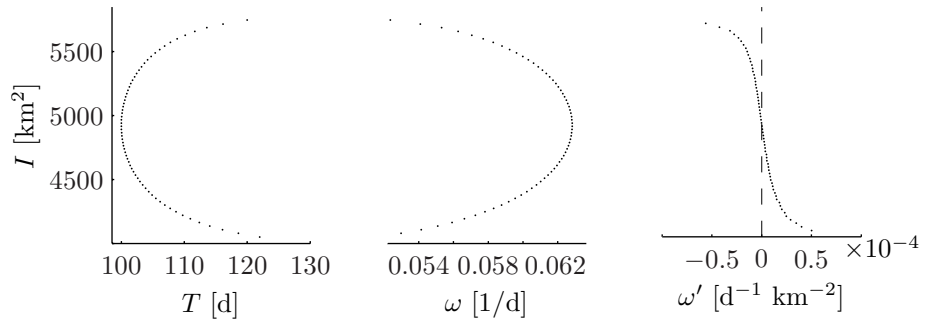

Figure 16: Plots of $T(I)$ (left), $\omega(I)$ (middle), and $\omega'(I)$ (right) for trajectories lying between the two homoclinic trajectories for the analytically described streamfunction, Eq. (109).

homoclinic trajectories is characterized by large value of shear. These observations will be important in the later discussion because it provides a basis for the "strong KAM stability" of tori near the shearless torus.

5.2 Qualitative behavior of an idealized steady three-gyre system under the influence of time-dependent perturbation

In this section we consider a general multiperiodic perturbation $\psi_1(x, y, t)$, denoted symbolically $\psi_1(x, y, \sigma_1 t, \sigma_2 t, \cdots, \sigma_N t)$, where the number of frequencies present, N, is assumed to be finite. The choice of a multiperiodic perturbation is made for two reasons. First, this class of perturbations is sufficiently general that one can argue that any time-dependent perturbation that is measured over a finite time interval (such as the one discussed in the following section, for example) can be accurately approximated as a multiperiodic function. In general the frequencies are incommensurable (not rationally related) and ψ_1 is a quasiperiodic function of t. The second reason for using multiperiodic perturbation is that rigorous mathematical results - a KAM theorem [44, 45, 46, 47], in particular (see Sec. 3.9 for details) - apply to

this class of problems. According to the KAM theorem for such systems [78, 47], for sufficiently small perturbation and assuming certain other conditions are satisfied, some unbroken tori exist in the perturbed system. These unbroken tori provide impenetrable transport barriers [49]. (This is because it can be shown that in the relevant higher dimensional phase space there is no Arnold diffusion as described in Sec. 3.9.)

We turn our attention now to the resonance width arguments and application of the strong KAM stability phenomenon to the perturbed three-gyre system. Recall from Fig. 16 that near the shearless torus $\mid \omega'(I) \mid$ is small. A simple analysis presented in Sec. 3.10 reveal that tori in the vicinity of the shearless torus are expected to be resistant to breaking due to the smallness of resonance widths (Eq. 86) in this region. Resonances are excited near the shearless torus, on which $\omega'(I) = 0$, but because resonance widths are generally very small, these resonances generally do not overlap. The arguments just given lead to the notion of strong KAM stability near shearless (also known as degenerate) tori [49, 7]. It is important to understand, however, that the stability of tori near the shearless torus is not absolute: these tori will break up either when a low-order resonance is excited in the close proximity of the shearless torus or when the strength of the perturbation ϵ overcomes the smallness of ω' in this region. The theoretical results just described lead to the expectation that a qualitative change in transport properties of the perturbed three-gyre system will occur as the perturbation strength exceeds a certain threshold. This change is associated with the breakup of the last surviving KAM torus in the vicinity of the

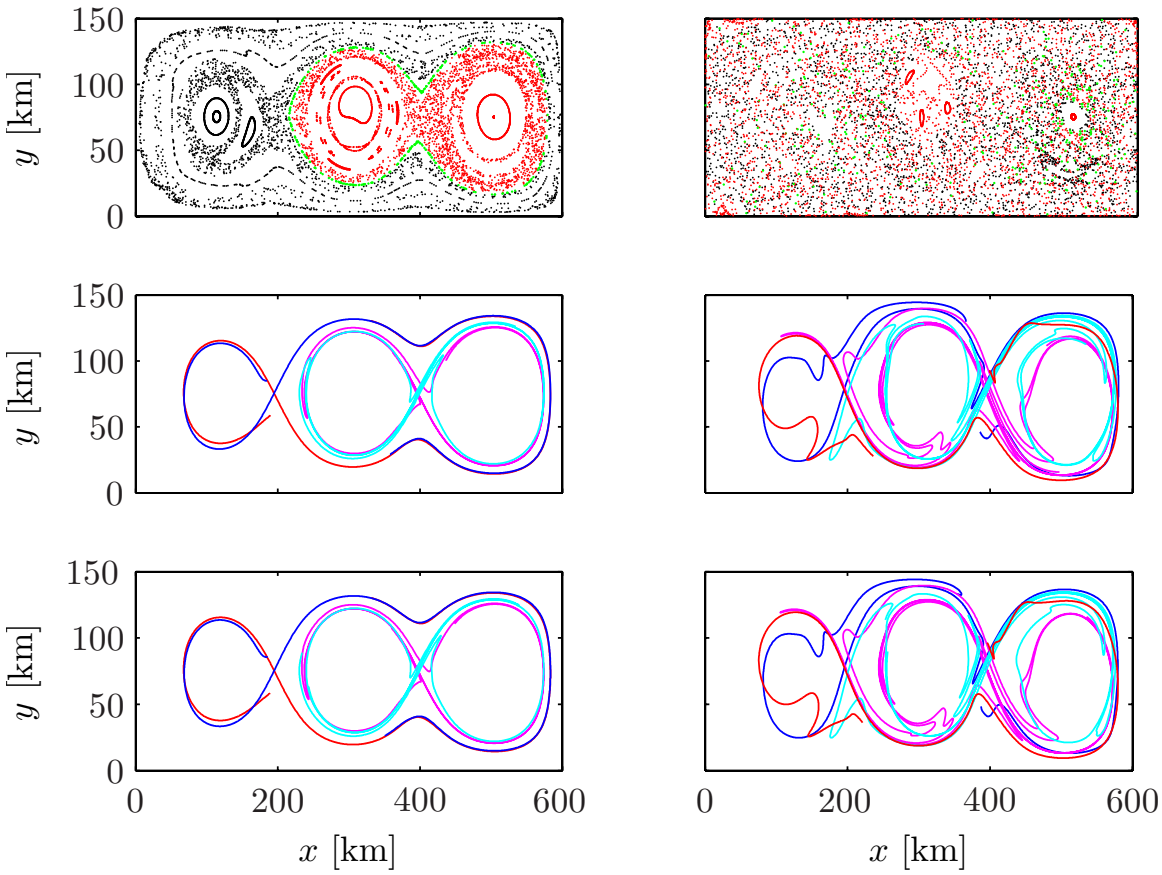

Figure 17: Simulations based on the system described by Eqs. (2, 108, 109, 110) for two values of ϵ: $\epsilon = 0.05$ on the left and $\epsilon = 0.3$ on the right. (Upper plots) Poincare sections for systems with a periodic perturbation comprised of a superposition of 14 standing waves whose frequencies are commensurable with a common period of 60 days. A KAM invariant torus is shown in green on the upper left subplot. Note that this closed curve serves as a transport barrier for the color-coded trajectories whose initial positions are inside (red dots) and outside (black dots) the closed curve. (Middle plots) Stable (blue and light blue curves) and unstable (red and pink curves) manifolds of nonstationary hyperbolic points for the same systems that were used to produce the upper plots. (Lower plots) Stable (blue and light blue curves) and unstable (red and pink curves) manifolds of nonstationary hyperbolic points for systems with a quasiperiodic perturbation comprised of a superposition of 14 standing waves whose frequencies are not commensurable.

shearless trajectory.

Some of the results just described are illustrated with numerical simulations that are shown in the upper panels of Fig. 17. These numerical simulations use the analytically prescribed streamfunction, Eq. 109, and assume a particular form of a

multiperiodic perturbation, consisting of a superposition of standing waves,

$$\psi_1(x,y,t) = \sum_{n,m} a_{nm} \cos(\sigma_{nm} t + \phi_{nm}) \sin(k_x^n x) \sin\left(k_y^m y\right) \tag{110}$$

with $k_x^n = \pi n/L_x$, $k_y^m = \pi m/L_y$ so that the boundary condition $\psi = 0$ at $x = 0$, $x = L_x$, $y = 0$ and $y = L_y$ is satisfied. The frequency spectrum is assumed to be red with $a_{nm} \sim \sigma_{nm}^{-1}$, and the wavenumber spectrum is assumed to be isotropic, $\sigma(\mathbf{k}) = \sigma(|\,\mathbf{k}\,|)$. The latter assumption together with geometrical dimensions of the basin, $L_x = 4L_y$, leads to degenerate frequencies defined by the condition $\sigma_{n_1,m_1} = \sigma_{n_2,m_2}$. For $n_{max} = 8$ and $m_{max} = 2$, which are used for modeling purposes, two degenerate frequencies are present. Thus, for the perturbation considered, 14 different frequencies σ_{nm} are present. For the numerical simulations shown here, the periods of standing waves in Eq. (110) were chosen to span the time interval from approximately 1 week to 2 months. Note that these periods are small compared to typical periods of rotation in the background flow - recall Fig. 15.

The upper panels of Fig. 17 are Poincare sections (see Sec. 3.2 for details). These can be constructed when the perturbation ψ_1 is periodic. To achieve this, the 14 standing wave periods were chosen to be commensurable with a common period of 60 days. This choice was made purely for the convenience of allowing Poincare sections to be made. It should be emphasized that the class of problems to which KAM theorems are known to apply is larger than the class of periodic perturbations. Relevant results are discussed in [46, 78, 79, 47]. This will not be discussed further except to note that in quasiperiodic systems (the general multiperiodic case) KAM

invariant tori undulate in time, undergoing what Jorba and Simo [78] refer to as a "quasiperiodic dance". Only in the special case of a periodic perturbation do the positions of the invariant tori (transport barriers) repeat themselves in a periodic fashion.

Consistent with the discussion above, Fig. 17 shows that for small ϵ some invariant tori (one such torus is shown in green in the upper left panel) in close proximity to the shearless torus provide an impenetrable transport barrier that separates the western gyre from the central and eastern gyre. There are seen to be two large figure-eight-shaped chaotic regions, one inside the eastern loop of the other, that do not overlap. For large ϵ the barrier between these figure-eight bands is broken and a large chaotic region that includes portions of all three gyres is present. This is illustrated in the upper right panel of Fig. 17.

Note also that, consistent with the resonance width analysis described in Sec. 3.10, trajectories near the homoclinic trajectories that are characterized by a very large value of ω' are the first to break under the perturbation.

Several techniques from dynamical systems theory - stable and unstable manifolds, lobe dynamics, LCSs - are suited for studying transport and mixing in systems with nonperiodic time dependence. These techniques are reviewed in Secs. 3.3, 3.4, 3.5, 3.7, and 3.11. We turn our attention now to the theory and applications of such dynamical systems tools.

In nonsteady flows chaotic transport of fluids is driven by stable and unstable manifolds of nonstationary hyperbolic points (or hyperbolic trajectories) - see Sec. 3.3. Stable and unstable manifolds are material curves and as such can not be traversed

by fluid particles. In nonsteady flows, stable and unstable manifolds intersect each other. Closed regions produced by segments of intersecting stable and unstable manifolds are called lobes. Lobes are important because fluid particles that are originally located inside the lobe are constrained to remain within the lobe as the flow evolves. When approaching the nonstationary hyperbolic point, stable and unstable manifolds and the associated lobes form complicated structures called homoclinic or heteroclinic tangles, which provide a template for chaotic mixing within the corresponding chaotic region.

The qualitative change in transport properties of the perturbed three-gyre system associated with the break up of the last surviving torus in the vicinity of the shearless trajectory must be accompanied by the qualitative change in the manifold structure. This is illustrated in the middle and lower panels of Fig. 17. This figure shows the manifold structure for the system (2, 108, 109, 110) with two values of ϵ: small ϵ ($\epsilon = 0.0.05$) on the left and large ϵ ($\epsilon = 0.3$) on the right. The two middle subplots of Fig. 17 correspond to the periodic perturbation ψ_1; the parameters used to produce the middle panels are identical to those used to produce the upper panels of Fig. 17. The two lower panels of Fig. 17 correspond to the quasiperiodic perturbation ψ_1; 14 periods of standing waves in Eq. (110) were chosen to be incommensurable and cover the time interval from approximately 7 days to 63 days.

In the left middle and left bottom panels of Fig. 17 (which correspond to small ϵ), stable and unstable manifolds associated with the same hyperbolic point intersect each other in the homoclinic manner. Associated with each of the two nonstationary hyperbolic points is a homoclinic tangle. Each homoclinic tangle provides a template

for chaotic mixing within the corresponding figure-eight-shaped chaotic band. No heteroclinic intersections are present. This is consistent with the notion that two figure-eight bands are separated from each other by an impenetrable barrier (an invariant KAM torus) and do not mix. In the right middle and right bottom panels of Fig. 17 (which correspond to large ϵ), the transport barrier is broken and both homoclinic and heteroclinic intersections between stable and unstable manifolds are present. Heteroclinic tangles and the associated heteroclinic lobes provide a template for fluid exchange between all three gyres. This is consistent with the upper right panel of Fig. 17 where one well-mixed chaotic region is seen that includes portions of all three gyres.

Due to time-periodicity of the perturbation, the manifold structure in the middle panels of Fig. 17 repeats itself after each period of the perturbation $2\pi/\sigma$. This is not true for the two lower panels of Fig. 17 where the manifold structure evolves in time in a non time-periodic fashion. The qualitative similarity between the left middle and left bottom panels of Fig. 17 (also, right middle and right bottom panels of Fig. 17) suggest that the details of the structure of the perturbation are less important than the geometry of the background streamfunction (such as existence of hyperbolic points, homoclinic trajectories and shearless trajectories) and the strength of the perturbation.

To summarize, the behavior of the steady three-gyre system under time-dependent perturbation is as follows. For small ϵ two nonoverlapping figure-eight-shaped chaotic regions, each with a crossing region that covers one of the nonstationary hyperbolic points, are present. The two figure-eights are separated from each other by an im-

penetrable transport barrier comprised of a thin band of KAM invariant tori in the vicinity of the shearless trajectory. Only manifold intersections of the homoclinic type are present. Under such conditions two of the gyres exchange no fluid with the third gyre. For large ϵ, the transport barrier associated with KAM invariant tori in the vicinity of the shearless torus is broken. The two chaotic figure-eight-shaped regions merge with each other and one chaotic region that includes portions of all three gyres is formed. Both homoclinic and heteroclinic intersections between stable and unstable manifolds are present. Under such conditions transport between all three gyres occurs.

5.3 Transport in an observationally-based three-gyre model

In this section an observationally-based model of the surface circulation of the Adriatic Sea is used to test whether qualitative features of the three-gyre system under perturbation can be identified in a more realistic setting. The observationally-based streamfunction has the form of Eq. (108) where $\psi_0(x,y)$ is the surface-drifter-derived mean streamfunction shown in Fig. 13 and $\psi_1(x,y,t)$ is a measured altimetric (sea level height) perturbation. To produce the perturbation field $\psi_1(x,y,t)$ a geostrophic balance is assumed to be satisfied so that $\psi_1 = \frac{g}{f}\eta$, where η is the sea level height and the coriolis parameter $f = 2\Omega \sin\phi$ is assumed to be constant. Knowledge of both $\psi_0(x,y)$ and $\psi_1(x,y,t)$ allows dependence on the perturbation strength ϵ in Eq. (108) to be explored. In our simulations $\epsilon = 1$ corresponds to the true perturbation strength. The measured altimetric perturbation field covers the time interval of one year, from 5 January 1993 (that corresponds to $t = 0$ days) to 6 January 1994

(that corresponds to $t = 365$ days) with $\Delta t = 7$ days. Measured altimetric height fields were modified in a thin boundary layer around the perimeter of the domain to enforce the condition $\psi_1 = \text{const}$ on the smoothed coastline. The relative strength of the background field compared to the perturbation field, i.e., the ratio of the time-averaged integrated kinetic energy associated with ψ_1 to the integrated kinetic energy associated with ψ_0, is 1.05.

Before proceeding some shortcomings of our observationally-based model of the surface circulation of the Adriatic Sea will be noted. First, the surface circulation in the Adriatic Sea is strongly influenced by intense short-lived Bora and Sirocco wind forcing events, during which the decomposition Eq. (108) is questionable [80]. Second, the measured altimetric (sea level height) perturbation is a measure of vertically integrated transport which need not coincide with near-surface transport. Third, the altimetric height field $\psi_1(x, y, t)$ does not resolve any submesoscale structure. And fourth, tide removal is difficult in enclosed basins such as the Adriatic, leading unavoidably to some aliasing of tidal energy into mesoscale fields. In spite of these caveats it should be emphasized that both $\psi_0(x, y)$ and $\psi_1(x, y, t)$ used here are observationally-based and their sum fairly accurately represents mesoscale near-surface current variability in the Adriatic Sea.

The altimetric perturbation field $\psi_1(x, y, t)$ is not a periodic function, so it is not possible to construct a Poincare section for the flow described by $\psi_0(x, y) + \epsilon\psi_1(x, y, t)$. However, the KAM-theory-based arguments presented in the previous section are still applicable if 1) $\langle\psi_1(x, y, t)\rangle = 0$ and 2) $\psi_1(x, y, t)$ can be accurately approximated by a multiperiodic sum with a finite number of terms. Both conditions

are expected to be satisfied. With this in mind, we expect that all of the important qualitative features of the perturbed three-gyre system that were discussed in the preceding section hold for the observationally-based system considered here. In particular, we seek to test whether the following qualitative features of the manifold and lobe structure, which were emphasized in the previous section, can be reproduced using the measured velocity fields: 1) for small ϵ all manifold intersections are of the homoclinic type and manifolds form two nonoverlapping figure-eight-shaped bands, each with a crossing region that covers one of the hyperbolic points; and 2) for large ϵ the transport barrier between the two figure eight bands is broken and heteroclinic manifold intersections are formed, thereby allowing transport between all three gyres.

Before proceeding we wish to emphasize that our concern is with the manifold structure associated with the basin-scale circulation in the Adriatic. This structure is linked to the two hyperbolic points that separate the three main gyres. We exclude from consideration more localized structures associated with the hyperbolic points near the northwestern end of the smoothed Adriatic domain (recall Fig. 13) that we are using, and the localized structures near the centers of the three main gyres. Also, under perturbation new hyperbolic points may form. For a weak perturbation, regions where ψ_0 is locally flat - near the centers of the main gyres, are most susceptible to this behavior. (Note also that the hyperbolic points need not coincide with the hyperbolic stagnation points of the flow, whose locations are sensitive to the choice of reference frame.) The manifolds associated with these localized structures are important locally but do not influence the larger scale intergyre transport that is the focus of our study.

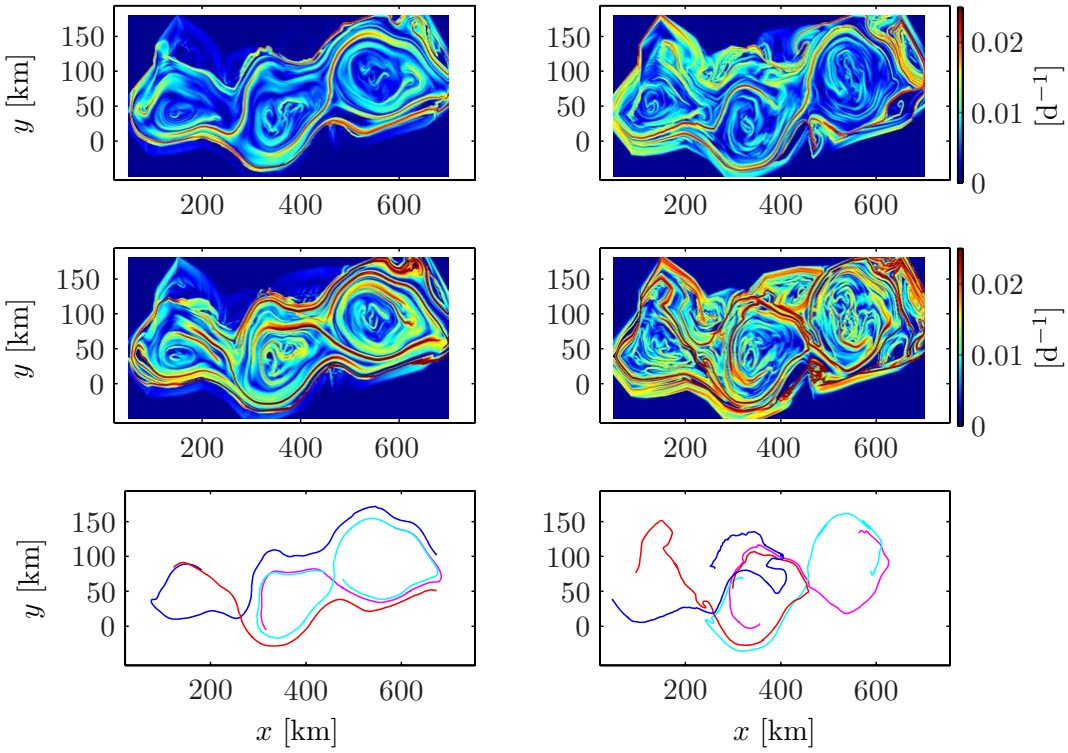

Figure 18: Simulations of stable and unstable manifolds using the observationally-based model of the Adriatic Sea for two values of the perturbation strength: $\epsilon = 0.1$ in the left panels and $\epsilon = 1$ in the right panels. (Upper panels) FTLE estimates computed in forward time relative to $t = 182$ days. Ridges of intense red correspond to stable manifolds. (Middle panels) FTLE estimates computed in backward time relative to $t = 182$ days. Ridges of intense red correspond to unstable manifolds. (Lower panels) Stable (red and pink curves) and unstable (blue and light blue curves) manifolds computed using the double time-slice method relative to $t = 182$ days. Note that the estimated structures of the stable and unstable manifolds computed using FTLEs and the double time-slice method are in excellent agreement.

Numerical simulations based on the observationally-based model described above are shown in Figs. 18, 19, 20 and 21. For two values of ϵ, small ϵ ($\epsilon = 0.1$) on the left and large ϵ ($\epsilon = 1$) on the right, stable and unstable manifolds of generaly nonstationary hyperbolic points are shown in Fig. 18. The upper four subplots of Fig. 18 show FTLE estimates computed in forward (upper two subplots) and backward (middle two subplots) time as a function of initial condition; regions of most intense red colors in the upper two subplots and in the middle two subplots of Fig. 18 correspond to

stable and unstable manifolds, respectively, of nonstationary hyperbolic points. The lower two subplots of Fig. 18 show segments of stable and unstable manifolds constructed using the double time-slice method described in Sec. 3.5. Unstable manifolds of the two hyperbolic points are shown using red and pink curves; stable manifolds are shown using blue and light blue curves. Note that manifold estimates computed as maximizing ridges of the FTLE field agree well with manifolds computed using the double time-slice method.

Consistent with the behavior of an idealized three-gyre system under perturbation and in qualitative agreement with Fig. 17, both methods serve to confirm that in the small ϵ case (left three panels of Fig. 18) all manifold intersections are of the homoclinic type. This strongly suggests the existence of two nonoverlapping figure eight bands of chaotic motion, each with a crossing region that covers one of the hyperbolic points. Chaotic motion inside each figure eight band is governed by lobes produced by homoclinic intersections of stable and unstable manifolds of the corresponding hyperbolic point. The absence of heteroclinic intersections indicates that the two figure-eight bands do not exchange fluid with each other and suggests the existence of a barrier to transport between the two figure-eights. In the large ϵ case, which is illustrated in the three right panels of Fig. 18, both methods produce manifold intersections of both the homoclinic and the heteroclinic type. It is the presence of the hetroclinic intersections and heteroclinic lobes that indicates a formation of one large chaotic region that includes portions of all three gyres. Heteroclinic lobes provide a template for gyre-to-gyre-to-gyre transport within this large chaotic region.

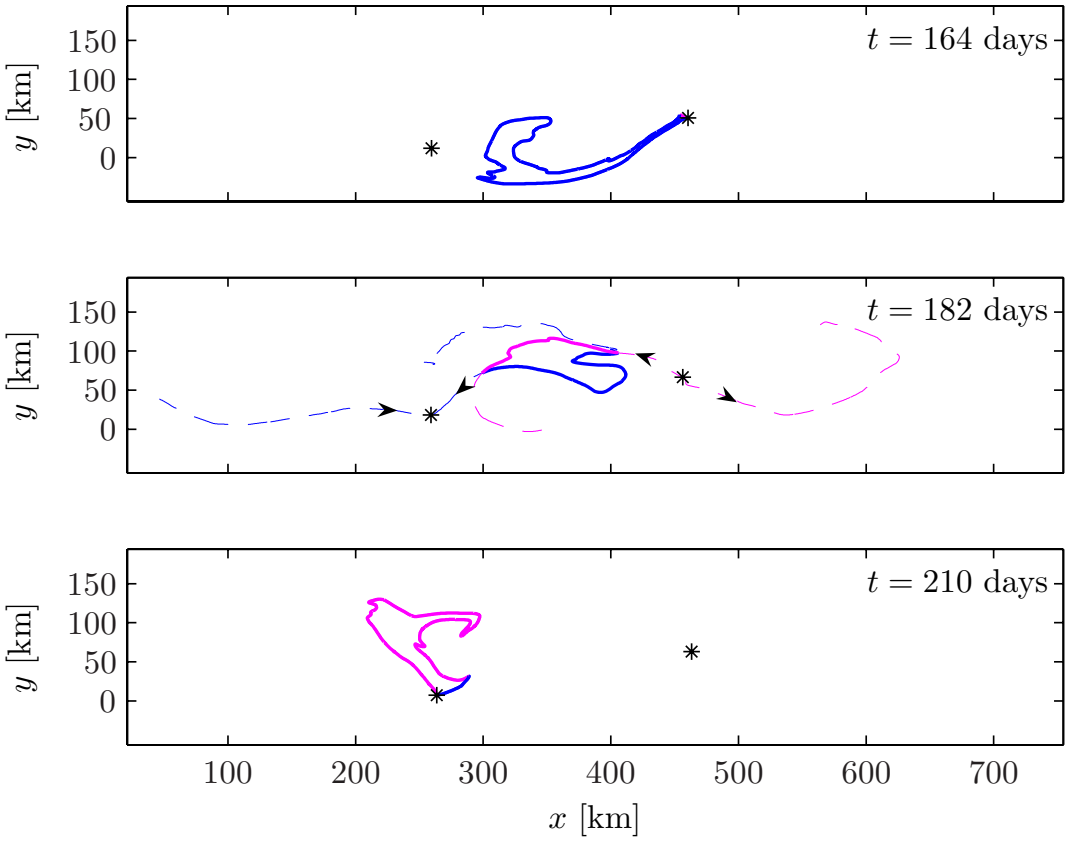

Figure 19: Simulations of the heteroclinic lobe evolution in forward and backward time relative to $t = 182$ days using the observationally-based model of the Adriatic Sea with the true value of the perturbation strength, $\epsilon = 1$. The boundary of the heteroclinic lobe is shown at the times indicated in the three panels. The portion of the boundary of the lobe that is comprised of a segment of the unstable manifold is shown in pink; the portion of the boundary of the lobe that is comprised of a segment of the stable manifold is shown in blue. Positions of the two (eastern and western) nonstationary hyperbolic points are shown with asterisks. In the middle subplot, the stable and unstable manifolds which form the heteroclinic lobe are shown by dashed blue and dashed pink lines. Arrows on the manifolds indicate the direction of attraction/repulsion.

The evolution of a heteroclinic lobe in forward and backward time is illustrated in Fig. 19, where the position of the heteroclinic lobe is shown at three different times, $t = 164$ days, $t = 182$ days and $t = 210$ days. To produce the upper and lower panels of Fig. 19, the heteroclinic lobe formed by stable and unstable manifolds at $t = 182$

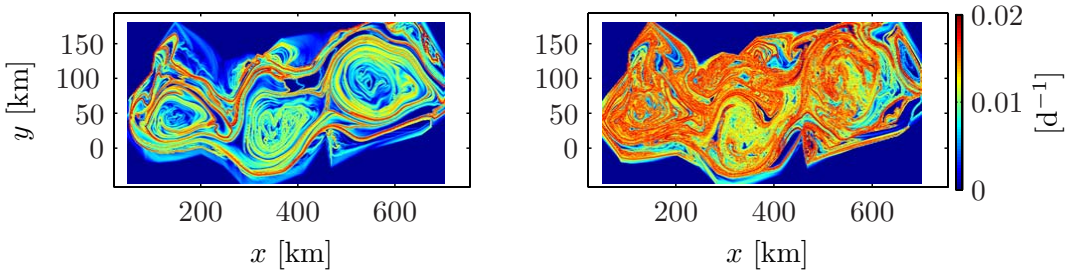

Figure 20: FTLE estimates for the observationally-based model of the Adriatic Sea surface circulation for two values of ϵ: (left) $\epsilon = 0.1$; (right) $\epsilon = 1$ (true perturbation strength). The integration interval is 120 days.

days (which is shown in the middle panel of this figure) was evolved backward and forward in time. Because stable and unstable manifolds are material lines and thus constitute impenetrable transport barriers, fluid particles initially located within the lobe are constrained to remain within the lobe as the flow evolves. From Fig. 19 it is seen that the segment of the stable manifold bounding the lobe decreases in length as time progresses as this segment approaches the western nonstationary hyperbolic point while the segment of the unstable manifold increases in length. In backward time, the segment of the stable manifold bounding the lobe increases in length while the segment of the unstable manifold decreases in length as this segment approaches the eastern nonstationary hyperbolic point. As a result, in forward/backard time lobes evolve into long filaments stretched in the direction of the unstable/stable manifold. This process leads to effective nonlocal stirring.

The FTLE-based detection scheme (described in Sec. 3.11) that was used to identify stable and unstable manifolds in Fig. 18 is also capable of identifying barriers to transport associated with surviving KAM invariant tori. However, in most cases, longer integration intervals are required for this task. (In particular, the integration time used to produced upper four panels of Fig. 18 is sufficient to give estimates of

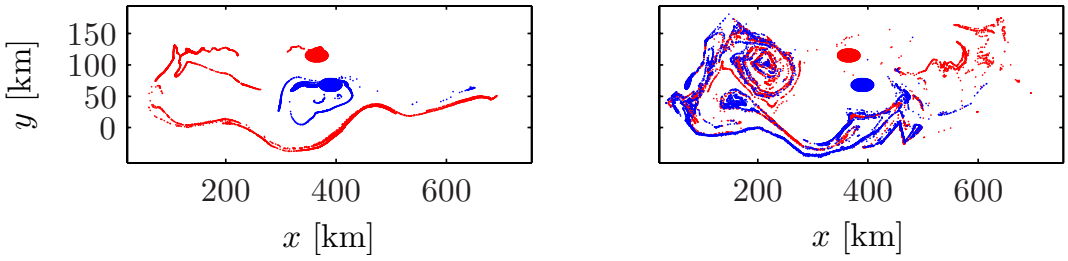

Figure 21: Initial (at $t = 182$ days) and final (at $t = 302$ days) position of two sets of passive tracers in the observationally-based model of the Adriatic Sea for two values of the perturbation strength: (left) $\epsilon = 0.1$; (right) $\epsilon = 1$. The initial positions of the two sets of tracers lie inside two circles and are shown in red and blue; the final positions of two sets of tracers are shown by red and blue dots, respectively.

stable and unstable manifolds but is not sufficient to detect a transport barrier near the shearless trajectory comprised of a thin band of surviving KAM tori.) The result of the FTLE computations with longer integration time is shown in Fig. 20. The region in the immediate vicinity of the shearless trajectory in the small ϵ case (left panel) is seen to be associated with a thin band of anomalously small Lyapunov exponents. This indicates regular (nonchaotic) motion in this region, which is associated with a transport barrier comprised of surviving KAM invariant tori. The right panel of Fig. 20 indicates that this barrier is broken when ϵ is increased.

A consequence of the two nonoverlapping figure eight chaotic regions that are separated from each other by an impenetrable transport barrier is that the distribution of passive tracers will be homogenized on each side of the barrier within each of the two figure eight bands. When the barrier is broken and the two figure eight bands merge forming one large chaotic region, the distribution of passive tracers will be homogenized within this large chaotic region. This behavior is illustrated in Fig. 21, which shows the initial (at $t = 182$ days) and final (at $t = 302$ days) positions of two sets of fluid particles for the observationally-based model with two values of ϵ, small

ϵ ($\epsilon = 0.1$) on the left and large ϵ ($\epsilon = 1$) on the right. For both values of ϵ the same initial positions of the two sets of fluid particles are used. Initial positions of the two sets are chosen to fall on two nonintersecting circles on opposite sides of the transport barrier in the vicinity of the shearless torus in the small ϵ case. In the small ϵ case, shown in the left panel of Fig. 21, after 120 days of integration the fluid inside each circle is well stirred, but there is no mixing between the two sets, due to the presence of the transport barrier. In the large ϵ case, shown in the right panel of Fig. 21, after 120 days the two sets of initially separated fluid particles are mixed with each other, as indicated by what appears to be random distributions of dots of two colors. This mixing is possible because of the absence of a transport barrier and is facilitated by heteroclinic tangles.

The observationally-based model of the surface circulation in the Adriatic Sea does not have periodic time dependence. Consequently, the quantitative features of Figs. 18 and 21 depend on the starting time and integration time used in numerical simulations. However, Figs. 18 and 21 are representative of typical behavior of the system under investigation.

5.4 Summary and conclusion

In this chapter we have studied the behavior of a steady three-gyre system under time-dependent perturbation with the aid of relevant dynamical systems results, in particular, KAM theory, stable and unstable manifolds, and lobe dynamics. An analytically specified model was introduced to illustrate the importance of LCSs and the manner in which they control transport. A fully observationally-based model of

the Adriatic Sea surface circulation was used to test the robustness of the qualitative features of a perturbed three-gyre system when applied to a more realistic fluid flow.

The behavior of a three-gyre system under time-dependent perturbation is shown to be qualitatively different for small and large perturbation: differences in transport properties, manifold structure, barriers to transport and intergyre transport were found. For small perturbation all manifold intersections are of the homoclinic type; homoclinic tangles are present but heteroclinic tangles do not form. A barrier to transport is present that insures that two of the gyres exchange no fluid with the third gyre. In other words, gyre-to-gyre-to-gyre transport is prohibited under these conditions. The existence of such a barrier is linked to strong KAM stability near shearless tori. This transport barrier breaks down when the perturbation reaches a critical value (which depends on both the background and the perturbation). For large perturbation, both homoclinic and heteroclinic manifold intersections are present; transport between all three gyres occurs. KAM theory arguments and lobe dynamics arguments are consistent with each other.

In most realistic oceanic and atmospheric problems, the full complexity of the flow can not be captured by available measurement techniques. Available numerical modeling schemes usually contain some missing physics as well. In this section, using the example of the surface circulation in the Adriatic Sea, we have shown that, even when $\psi(x, y, t)$ is not known exactly, the dynamical systems approach allows one to obtain important qualitative information about the system under investigation.

6 Summary

The work reported here is concerned with understanding transport and mixing in two-dimensional and incompressible oceanic and atmospheric fluid flows. The associated Lagrangian dynamics was studied with the aid of dynamical systems techniques: KAM theory, stable and unstable manifold structure, and lobe dynamics. The Hamiltonian structure of the Lagrangian equations of motion has been exploited extensively in our studies.

Much of the work focused on the role of transport barriers, their underlying dynamics, and methods of their identification. In the theory of dynamical systems, transport barriers in nonsteady 2D incompressible flows can be characterized as LCSs. Identification of LCSs is generally not possible from naked eye inspection of Eulerian velocity fields and requires the use of dynamical systems techniques. Two types of LCSs are of primary importance: 1) stable and unstable manifolds of generally nonstationary hyperbolic points; and 2) invariant KAM tori, the existence of which is predicted by the KAM theorem provided the flow of interest satisfies certain conditions. Because both types of structures are material lines of fluid they can not be traversed by, and therefore strongly constrain the motion of, neighboring fluid particles. Stable and unstable manifolds in nonsteady flows are involved in facilitating efficient transport in regions with chaotic behavior, while KAM invariant tori provide barriers to transport. Transport barriers associated with KAM invariant tori are often found near cores of jet-like structures in the flow of interest due to the strong KAM stability phenomenon.

The complementary nature of the KAM theory and stable and unstable manifold structure has been emphasized. In particular, the presence of KAM invariant tori in the system imposes strong constraints on the corresponding stable and unstable manifold structure. One such constraint is that in regions where stable and unstable manifold intersections are formed, KAM invariant tori can not be present. Also, resonance widths arguments, which lead to strong KAM stability near shearless tori, predict that tori near the homoclinic and heteroclinic trajectories are the first to break under the perturbation. This provides an alternate explanation of well-known results from lobe dynamics theory, which predicts that in nonsteady flows stable and unstable manifolds generally do not coincide with each other; instead they intersect transversally forming lobes that govern transport in regions with chaotic behavior.

Two applications, one atmospheric and one oceanic, were considered in the work presented. The first application considered concerns with the Lagrangian dynamics of the zonal jet at the perimeter of the Stratospheric Polar Vortex, which forms over Antarctica in the late winter/early spring. A dynamically-motivated model was employed in these studies. A robust transport barrier of the strong KAM stability type was found near the core of the zonal jet under typical late winter/early spring conditions. This type of barrier provides the trapping mechanism which keeps ozone-depleted air within the ozone hole. Causes for the breakdown of such a barrier were discussed. Our strong KAM stability explanation for the transport barrier at the perimeter of the ozone hole was contrasted to the potential vorticity barrier explanation. Recent work on transport barriers in planetary atmospheres [13] reveals that, consistent with our strong KAM stability arguments but conflicting with the potential

vorticity barrier arguments, both eastward and westward zonal jets serve as robust meridional transport barriers in the atmosphere of Jupiter. The flow considered in [13] provides an example of a dynamically-consistent flow where transport barriers are present that are not associated with a jump in potential vorticity.

The second application considered was concerned with intergyre transport in a perturbed three-gyre system. The study of this problem was motivated by the observations of surface drifters in the Adriatic Sea, which suggest the presence of a robust three-gyre background flow pattern. It was shown that the behavior of the perturbed three-gyre system is qualitatively different for small and for large perturbation. For small perturbation, a transport barrier of the strong KAM stability type is present, which separates two gyres from the third gyre, so that two of the gyres exchange no fluid with the third gyre. Under such conditions all stable and unstable manifold intersections are of the homoclinic type. After the perturbation reaches a certain threshold, the transport barrier of the strong KAM stability type is broken, heteroclinic intersections between stable and unstable manifolds form and transport between all three gyres occurs. This behavior was shown to be predicted theoretically, and was illustrated using an analytically prescribed model and then tested in a more realistic setting using a fully observationally-based model of the surface circulation in the Adriatic Sea.

Our work on the perturbed three-gyre system is important as a first step towards understanding transport and mixing in more realistic multiple-gyre systems. Motivated by the obtained results on the perturbed three-gyre system, we expect that finite amplitude bifurcations will occur in perturbed multiple-gyre systems as

the perturbation strength increases. Similarly to the perturbed three-gyre system, these bifurcations are associated with the break up of transport barriers of the strong KAM stability type, the formation of heteroclinic tangles and appearance of intergyre transport between gyres that exchanged no fluid with each other for smaller values of the perturbation. It is the presence of heteroclinic tangles that allows for efficient nonlocal stirring of fluid.

References

[1] G. Haller. Finding finite-time invariant manifolds in two-dimensional velocity fields. *Chaos*, 10:99–108, 2000.

[2] G. Haller and G. Yuan. Lagrangian coherent structures and mixing in two-dimensional turbulence. *Physica D*, 147:352–370, 2000.

[3] G. Haller. Distinguished material surfaces and coherent structures in 3D fluid flows. *Physica D*, 149:248–277, 2001.

[4] G. Haller. Lagrangian structures and the rate of strain in a partition of two-dimensional turbulence. *Phys. Fluids*, 13:3365–3385, 2001.

[5] G. Haller. Lagrangian coherent structures from approximate velocity data. *Physics Fluid*, 14:1851–1861, 2002.

[6] F. Lekien, C. Coulliette, A. J. Mariano, E. H. Ryan, L. K. Shay, G. Haller, and J. E. Marsden. Pollution release tied to invariant manifolds: A case study for the coast of Florida. *Physica D*, 210:1–20, 2005.

[7] I. I. Rypina, M. G. Brown, F. J. Beron-Vera, H. Kocak, M. J. Olascoaga, and I. A. Udovydchenkov. Robust transport barriers resulting from strong Kolmogorov-Arnold-Moser stability. *Phys. Rev. Lett.*, 98:10.1103/PhysRevLett.98.104102, 2007.

[8] M. J. Olascoaga, I. I. Rypina, M. G. Brown, F. J. Beron-Vera, H. Kocak, L. E. Brand, G. R. Halliwell, and L. K. Shay. Persistent transport barrier on the West Florida Shelf. *Geophys. Res. Lett.*, 33:doi:10.1029/2006GL027800, 2006.

[9] S. Wiggins. The dynamical systems approach to Lagrangian transport in oceanic flows. *Annu. Rev. Fluid Mech.*, 37:295–328, 2005.

[10] C. Coulliette and S. Wiggins. Intergyre transport in a wind-driven, quasi-geostrophic double gyre: An application of lobe dynamics. *Nonlin. Proc. Geophys.*, 8:69–94, 2001.

[11] P. D. Miller, C. K. R. T. Jones, A. M. Rogerson, and L. J. Pratt. Quantifying transport in numerically generated velocity fields. *Physica D*, 110:105–122, 1997.

[12] P. D. Miller, L. J. Pratt, K. R. Helrich, and C. K. R. T. Jones. Chaotic transport of mass and potential vorticity for an island recirculation. *J. Phys. Oceanogr.*, 32:80–102, 2002.

[13] F. J. Beron-Vera, M. G. Brown, M. J. Olascoaga, I. I. Rypina, H. Kocak, and I. A. Udovydchenkov. Zonal jets as transport barriers in planetary atmospheres. *Geophys. Res. Lett., submitted*, 2007.

[14] O. Cardoso, B. Gluckmann, O. Parcollet, and P. Tabeling. Dispersion in a quasi-two-dimensional-turbulent flow: An experimental study. *Phys. Fluids*, 8 (1):209–214, 1996.

[15] O. Cardoso and P. Tabeling. Anomalous diffusion in a linear array of vortices. *Europhys. Letters*, 7:225–230, 1988.

[16] O. Cardoso and P. Tabeling. Anomalous diffusion in a linear system of vortices. *Eur. j. mech. B, Fluids*, 8 (6):459–470, 1989.

[17] T. H. Solomon and J. P. Gollub. Passive transport in steady Rayleigh-Benard convection. *Phys. Fluids*, 31:1372–1379, 1988.

[18] T. H. Solomon and J. P. Gollub. Chaotic particle transport in time-dependent Rayleigh-Benard convection. *Phys. Rev. A*, 38:6280 – 6286, 1988.

[19] C. Eckart. An analysis of the stirring and mixing processes in incompressible fluids. *J. Mar. Res.*, 7:265–275, 1948.

[20] L. C. Evans. An introduction to stochastic differential equations. version 1.2. http://math.berkeley.edu/ evans/SDE.course.pdf (last visited 24-Sep-2007).

[21] L. Arnold. *Stochastic Differential Equations: Theory and Applications*. Wiley, New York, 1974.

[22] A. N. Borodin and P. Salminen. *Handbook of Brownian Motion - Facts and Formulae*. Birkhauser, 2 edition, 2002.

[23] H. McKean. *Stochastic Integrals*. Academic Press, 1969.

[24] D. J. Thomson. A random walk model of dispersion in turbulent flows and its applicability to dispersion in a valley. *Quat. J. R. Met. Soc.*, 112:511–529, 1986.

[25] A. Griffa. Applications of stochastic particle models to oceanographic problems. In R. J. Adler, P. Müller, and B. L. Rozovoskii, editors, *Stochastic Modelling in Physical Oceanography*, pages 114–140. Birkhäuser, 1996.

[26] S. Castellari, A. Griffa, T. M. Ozkomen, and P.-M. Poulain. Prediction of particle trajectories in the Adriatic Sea using Lagrangian data assimilation. *J. Mar. Syst.*, 29:33–50, 2001.

[27] A. Maurizi, A. Griffa, P.-M. Poulain, and F. Tampieri. Lagrangian turbulence in the Adriatic Sea as computed from drifter data: Effects of inhomogeneity and nonstationarity. *J. Geophys. Res.*, 109:doi:10.1029/2003JC002119, 2004.

[28] P.-M. Poulain. Adriatic Sea surface circulation as derived from drifter data between 1990 and 1999. *J. Marine Systems*, 29:3–32, 2001.

[29] A. C. Haza, L. I. Piterbarg, P. Martin, T. M. Ozgokmen, and A. Griffa. A Lagrangian subgridscale model for particle transport improvement and application in the Adriatic Sea using the Navy Ocean Model. *Ocean Modelling*, 17:68–91, 2007.

[30] L. D. Landau and E. M. Lifshitz. *Mechanics*. Pergamon, 3rd edition, 1976.

[31] S. Wiggins. *Chaotic Transport in Dynamical Systems*. Springer, 1992.

[32] V. Rom-Kedar and S. Wiggins. Transport in two-dimensional maps. *Arch. Rational Mech. Anal.*, 109:239–298, 1990.

[33] V. Rom-Kedar., A. Leonard, and S. Wiggins. An analytical study of transport, mixing, and chaos in an unsteady vortical flow. *J. Fluid Mech.*, 214:347–394, 1990.

[34] N. Malhotra and S. Wiggins. Geometric structures, lobe dynamics, and Lagrangian transport in flows with aperiodic time-dependence, with applications to Rossby wave flow. *J. Nonlinear Sci.*, 8:401–456, 1998.

[35] Y. Yi. A generalized integral manifold theorem. *J. Diff. Eq.*, 102:153–187, 1993.

[36] V. K. Melnikov. On the stability of the center for time periodic perturbations. *Trans. Mosc. Math. Soc.*, 12:1–57, 1963.

[37] T. J. Kaper, G. Kovacic, and S. Wiggins. Melnikov functions, action, and lobe area in Hamiltonian systems. *Los Alamos National Laboratory Technical Report. LA-UP 90-2455*, 1990.

[38] T. S. Parker and L. O. Chua. *Practical Numerical Algorithms for Chaotic Systems*. Springer, 1989.

[39] V. I. Arnold. *Mathematical Methods of Classical Mechanics*. Springer, 2nd edition, 1989.

[40] M. Tabor. *Chaos and Integrability in Nonlinear Dynamics*. John Wiley and Sons, 1989.

[41] M. A. Wolfson and S. Tomsovic. On the stability of long-range sound propagation through a structured ocean. *J. Acoust. Soc. Am.*, 109:2,693–2,703, 2001.

[42] F. J. Beron-Vera and M. G. Brown. Ray stability in weakly range-dependent sound channels. *J. Acoust. Soc. Am.*, 114:123–130, 2003.

[43] M. G. Brown. Phase space structure and fractal trajectories in $1\frac{1}{2}$ degree of freedom Hamiltonian systems whose time dependence is quasiperiodic. *Nonlin. Proc. Geophys.*, 5:69–74, 1998.

[44] A. N. Kolmogorov. On the persistence of conditionally periodic motions under a small change of the Hamilton function. *Dokl. Akad. Nauk SSSR*, 98:525–530, 1954. Engl. transl. *in* G. Casati and J. Ford (eds), Stochastic Behavior in Classical and Quantum Hamiltonian Systems, *Lect. Notes Physics* **93**: 51–56 (1979).

[45] V. I. Arnold. Proof of a theorem of A. N. Kolmogorov on the persistence of quasi-periodic motions under small perturbations of the Hamiltonian. *Russ. Math. Surveys*, 18:9–36, 1963.

[46] H. Rüssmann. Non-degeneracy in the perturbation theory of integrable dynamical systems. In M. M. Dodson and J. A. G. Vickers, editors, *Number Theory and Dynamical Systems*, pages 5–18. London Math. Soc. Lect. Notes Series, Cambridge University, 1989.

[47] M. B. Sevryuk. Invariant tori in quasi-periodic non-autonomous dynamical systems via Herman's method. *Dis. Cont. Dyn. Sys.*, 18:569–595, 2007.

[48] A. D. Bruno. On conditions for nondegeneracy in Kolmogorov's theorem. *Soviet Math. Dokl.*, 45:221–225, 1992.

[49] I. I. Rypina, M. G. Brown, F. J. Beron-Vera, H. Kocak, M. J. Olascoaga, and I. A. Udovydchenkov. On the Lagrangian dynamics of atmospheric zonal jets and the permeability of the stratospheric polar vortex. *J. Atmos. Sci.*, 64:3593–3610, 2007.

[50] J. Koiller, R. Markarian, S. Oliffson-Kamphorst, and S. P. de Carvalho. Time-dependent billiards. *Nonlinearity*, 8:983–1003, 1995.

[51] G. M. Zaslavsky, M. Yu. Zakharov, R. Z. Sagdeev, D. A. Usikov, and A. A. Chernikov. Stochastic web and diffusion of particles in a magnetic field. translated from zh. eksper. teoret fiz., 91, 500-516. *Sov. Phys. JETP*, 64:294–303, 1986.

[52] W. T. Kyner. Rigorous and formal stability of orbits about an oblate planet. *Mem. Am. Math. Soc.*, 81:1–27, 1968.

[53] A. Munteanu, E. Petrisor, E. Garcia-Berro, and J. Jose. Creation of twistless circles in a model of stellar pulsations. *Communications in Nonlinear Science and Numerical Simulation*, 8:355–373, 2003.

[54] G. A. Oda and I. L. Caldas. Dimerized island chains in tokamaks. *Chaos, Solitons and Fractals*, 5:15–23, 1995.

[55] M. G. Brown, J. A. Colosi, S. Tomsovic, A. L. Virovlyansky, M. Wolfson, and G. M. Zaslavsky. Ray dynamics in long-range deep ocean sound propagation. *J. Acoust. Soc. Am.*, 113:2533–2547, 2003.

[56] D. del-Castillo-Negrete and P. J. Morrison. Chaotic transport by Rossby waves in shear flow. *Phys. Fluids A*, 5(4):948–965, 1993.

[57] B. V. Chirikov. A universal instability of many-dimensional oscillator systems. *Phys. Rep.*, 52:265–379, 1979.

[58] B. V. Chirikov and G. M. Zaslavsky. Stochastic instability of nonlinear oscillations. *Sov. Phys. Usp.*, 14:549–672, 1972.

[59] A. G. Lichtenberg and M. A. Lieberman. *Regular and Stochastic Motion*. Springer, New York, 1983.

[60] G.M. Zaslavsky. *Chaos in Dynamic Systems*. Harwood Academic Publishers, NY, 1985.

[61] S. C. Shadden, F. Lekien, and J. E. Marsden. Definition and properties of Lagrangian coherent structures from finite-time Lyapunov exponents in two-dimensional aperiodic flows. *Physica D*, 212:271–304, 2005.

[62] S. C. Shadden, J. O. Dabiri, and J. E. Marsden. Lagrangian analysis of fluid transport in empirical vortex ring flows. *Phys. Fluids*, 18:47105, 2006.

[63] S. Kovalyov. Phase space structure and anomalous diffusion in a rotational fluid experiment. *Chaos*, 10:153–165, 2000.

[64] F.B. Lipps. The barotropic stability of the mean winds in the atmosphere. *J. Fluid Mech.*, 12:397–407, 1962.

[65] K. P. Bowman. Rossby wave phase speeds and mixing barriers in the stratosphere. Part I: Observations. *J. Atmos. Sci.*, 53:905–916, 1996.

[66] M. E. McIntyre. On the Antarctic ozone hole. *J. Atmos. Terr. Phys.*, 51:29–43, 1989.

[67] N. M. Juckes and M. E. McIntyre. A high-resolution one-layer model of breaking planetary waves in the stratosphere. *Nature*, 328:590–596, 1987.

[68] D. G. Dritchel, P. H. Haynes, and M. E. McIntyre. Multiple jets as PV staircases: the Phillips effect and the resilience of eddy-transport barriers. J. Atmos. Sci., *submitted*, 2006.

[69] G Falkovich, K. Gawedzki, and M. Vergassola. Particles and fields in fluid turbulence. *Rev. Mod. Phys.*, 73:913–975, 2001.

[70] M Orlic, M. Gacic, and P. E. La Violette. The currents and circulation of the Adriatic Sea. *Oceanol. Acta.*, 15:109–124, 1992.

[71] P. Falco, A. Griffa, P.-M. Poulain, and E. Zambianchi. Transport properties of the Adriatic Sea as deduced from drifter data. *J. Phys. Oceanogr.*, 30:2055–2071, 2000.

[72] A. Artegiani, D. Bregant, E. Pashini, N. Pinardi, F. Raicich, and A. Russo. The Adriatic Sea general circulation: Part I. Air-sea interactions and water mass structure. *J. Phys. Oceanogr.*, 27:1492–1514, 1997.

[73] A. Artegiani, D. Bregant, E. Pashini, N. Pinardi, F. Raicich, and A. Russo. The Adriatic Sea general circulation: Part II. Baroclinic circulation structure. *J. Phys. Oceanogr.*, 27:1515–1532, 1997.

[74] P.-M. Poulain. Drifter observations of surface circulation in the Adriatic Sea between December 1994 and March 1996. *J. Mar. Syst.*, 20:231–253, 1999.

[75] P.-M. Poulain, M Gacic, and B. Cushman-Rosin. *Physical Oceanography of the Adriatic Sea: Past, Present and Future*. Kluwer Academic Publishing, Dordrecht, The Netherlands, 2001.

[76] G. Lacorata, E. Aurell, and A. Vulpiani. Drifter dispersion in the Adriatic Sea: Lagrangian data and chaotic model. *Annales Geophys.*, 19:121–129, 2001.

[77] A. C. Haza, A. Griffa, A. Molcard, T. M. Ozgokmen, A. C. Poje, R. Barbanti, J. W. Book, P. M. Poulain, M. Rixen, and P. Zanasca. Model-based directed drifter launches in the Adriatic Sea: Results from DART experiment. *Geophys. Res. Lett.*, 34:L10605, 2007.

[78] Á Jorba and C. Simó. On quasi-periodic perturbations of elliptic equilibrium points. *SIAM J. Math. Anal.*, 27:1,704–1,737, 1996.

[79] C. Simó. Invariant curves of analytic perturbed nontwist area preserving maps. *Regul. Chaotic Dyn.*, 3(3):180–195, 1998.

[80] L. Ursella, P. M. Poulain, and R. P. Signell. Surface drifter derived circulation in the northern and middle Adriatic Sea: Response to wind regime and season. *Journal of Geophys Res.*, 112, C03S04, doi:10.1029/2005JC003177, 2007.